

# **High Energy Gamma-rays from Active Galactic Nuclei**



# Contents

<b>1 Topics</b>	<b>5</b>
1.1 ICRA-Net participants . . . . .	5
1.2 Students . . . . .	5
1.3 Ongoing collaborations . . . . .	6
<b>2 Brief description</b>	<b>7</b>
<b>3 Publications-2017</b>	<b>9</b>
3.1 Publications-2012-2017 . . . . .	10
<b>4 Lepto-hadronic <math>\gamma</math>-ray and neutrino emission from the jet of TXS 0506+056</b>	<b>13</b>
4.1 Introduction . . . . .	13
4.2 Broadband emission from jets . . . . .	15
4.2.1 The model . . . . .	16
4.3 SED modeling . . . . .	18
4.4 Results and Discussions . . . . .	20
4.5 Conclusions . . . . .	23
<b>5 On the multi-wavelength Emission from CTA 102</b>	<b>25</b>
5.1 Introduction . . . . .	25
5.2 Observations and Data Reduction . . . . .	28
5.2.1 Gamma-ray observations: Fermi LAT . . . . .	28
5.2.2 Swift UVOT/XRT observations . . . . .	31
5.2.3 NuSTAR observation . . . . .	32
5.2.4 The light curves variability . . . . .	32
5.3 Spectral evolution . . . . .	35
5.3.1 Spectral analysis . . . . .	36
5.4 Broadband SEDs . . . . .	38
5.4.1 Modeling the SEDs . . . . .	39

## *Contents*

---

5.5	Results and Discussion . . . . .	40
5.5.1	The origin of the emission . . . . .	41
5.6	Conclusions . . . . .	44
<b>6</b>	<b>Dissecting the region around IceCube-170922A: the blazar TXS 0506+056 as the first cosmic neutrino source</b>	<b>45</b>
6.1	Introduction . . . . .	45
6.2	Multi-messenger data analysis . . . . .	48
6.2.1	Neutrino data . . . . .	48
6.2.2	Radio and optical monitoring data . . . . .	49
6.2.3	X-ray and optical/UV data . . . . .	49
6.2.4	$\gamma$ -ray data . . . . .	51
6.3	Putting it all together . . . . .	54
6.3.1	Relevant astronomical sources in the region of IceCube-170922A . . . . .	54
6.3.2	$\gamma$ -ray emission near IceCube-170922A . . . . .	56
6.3.3	$\gamma$ -ray light curves . . . . .	57
6.3.4	Spectral energy distributions . . . . .	62
6.4	Results . . . . .	65
6.5	Discussion . . . . .	66
6.5.1	Source properties . . . . .	66
6.5.2	Physical implications . . . . .	67
6.5.3	Future searches . . . . .	68
6.6	Conclusions . . . . .	69

# 1 Topics

- High energy gamma-rays from active galactic nuclei
- Galactic sources of high energy neutrinos
- High energy emission from gamma-ray bursts

## 1.1 ICRANet participants

- Sahakyan Narek

## 1.2 Students

- Gasparyan Sargis
- Karlica Mile
- Mkrtchyan Tatevik
- Harutyunyan Gevorg
- Israyelyan Davit
- Khachatryan Mher
- Zargaryan David <sup>1</sup>
- Baghmanyanyan Vardan <sup>1</sup>
- Tumanyan Meri <sup>1</sup>

---

<sup>1</sup>Already left the group

### **1.3 Ongoing collaborations**

- Razmik Mirzoyan (Max Planck Institute for Physics, Munich, Germany)
- Paolo Giommi (ASI Science Data Center)
- Ulisses Barres de Almeida (Centro Brasileiro de Pesquisas Fisicas - CBPF/MCT)
- Bernardo Fraga (Centro Brasileiro de Pesquisas Fisicas - CBPF)

## 2 Brief description

The main scientific activities of our group are in the field of X- and gamma-ray Astrophysics and Astroparticle physics. The results from the data analysis of Swift UVOT/XRT, NuStar, Chandra and Fermi LAT telescopes are used to investigate the particle acceleration and emission processes in the different classes of active galactic nuclei. The analysis of available data allows to investigate the emission processes and relativistic outflows in the most extreme regimes (keV-TeV).

Below we present several abstracts from the papers published in 2018.

- Lepto-hadronic  $\gamma$ -ray and neutrino emission from the jet of TXS 0506+056

The observation of IceCube-170922A event from the direction of TXS 0506+056 when it was in its enhanced  $\gamma$ -ray emission state offers a unique opportunity to investigate the lepto-hadronic processes in blazar jets. Here, the observed broadband emission of TXS 0506+056 is explained by boosted synchrotron/synchrotron self Compton emission from the jet whereas the  $\gamma$ -ray data observed during the neutrino emission- by inelastic interactions of the jet-accelerated protons in a dense gaseous target. The proton energy distribution is  $\sim E_p^{-2.50}$ , calculated straightforwardly from the data obtained by Fermi-LAT and MAGIC and if such distribution continues up to  $E_{c,p} = 10$  PeV, the expected neutrino rate is as high as  $\sim 0.46$  events during the long active phase of the source or  $\sim 0.15$  if the activity lasts 60 days. In this interpretation, the energy content of the protons above  $>$  GeV in blazar jets can be estimated as well: the required proton injection luminosity is  $\simeq 2.0 \times 10^{48} \text{ erg s}^{-1}$  exceeding  $10^3$  times that of electrons  $\simeq 10^{45} \text{ erg s}^{-1}$  which are in equipartition with the magnetic field. As the required parameters are physically realistic, this can be an acceptable model for explanation of the neutrino and  $\gamma$ -ray emission from TXS 0506+056.

- On the multi-wavelength Emission from CTA 102

## 2 Brief description

---

We report on broadband observations of CTA 102 ( $z = 1.037$ ) during the active states in 2016-2017. In the  $\gamma$ -ray band, Fermi LAT observed several prominent flares which followed a harder-when-brighter behavior: the hardest photon index  $\Gamma = 1.61 \pm 0.10$  being unusual for FSRQs. The peak  $\gamma$ -ray flux above 100 MeV  $(3.55 \pm 0.55) \times 10^{-5} \text{ photon cm}^{-2} \text{ s}^{-1}$  observed on MJD 57738.47 within 4.31 minutes, corresponds to an isotropic  $\gamma$ -ray luminosity of  $L_\gamma = 3.25 \times 10^{50} \text{ erg s}^{-1}$ , comparable with the highest values observed from blazars so far. The analyses of the Swift UVOT/XRT data show an increase in the UV/optical and X-ray bands which is contemporaneous with the bright  $\gamma$ -ray periods. The X-ray spectrum observed by Swift XRT and NuSTAR during the  $\gamma$ -ray flaring period is characterized by a hard photon index of  $\sim 1.30$ . The shortest e-folding time was  $4.08 \pm 1.44$  hours, suggesting a very compact emission region  $R \leq \delta \times 2.16 \times 10^{14} \text{ cm}$ . We modeled the spectral energy distribution of CTA 102 in several periods (having different properties in UV/optical, X-ray and  $\gamma$ -ray bands) assuming a compact blob inside and outside the BLR. We found that the high-energy data are better described when the infrared thermal radiation of the dusty torus is considered. In the flaring periods when the correlation between the  $\gamma$ -ray and UV/optical/X-ray bands is lacking, the  $\gamma$ -ray emission can be produced from the interaction of fresh electrons in a different blob, which does not make a dominant contribution at lower energies.

- Dissecting the region around IceCube-170922A: the blazar TXS 0506+056 as the first cosmic neutrino source

We present the dissection in space, time, and energy of the region around the IceCube-170922A neutrino alert. This study is motivated by: (1) the first association between a neutrino alert and a blazar in a flaring state, TXS 0506+056; (2) the evidence of a neutrino flaring activity during 2014–2015 from the same direction; (3) the lack of an accompanying simultaneous  $\gamma$ -ray enhancement from the same counterpart; (4) the contrasting flaring activity of a neighbouring bright  $\gamma$ -ray source, the blazar PKS 0502+049, during 2014–2015. Our study makes use of multi-wavelength archival data accessed through Open Universe tools and includes a new analysis of Fermi-LAT data. We find that PKS 0502+049 contaminates the  $\gamma$ -ray emission region at low energies but TXS 0506+056 dominates the sky above a few GeV. TXS 0506+056, which is a very strong (top percent) radio and  $\gamma$ -ray source, is in a high  $\gamma$ -ray state during the neutrino alert but in a low though hard  $\gamma$ -ray state in coincidence

---

with the neutrino flare. Both states can be reconciled with the energy associated with the neutrino emission and, in particular during the low/hard state, there is evidence that TXS 0506+056 has undergone a hadronic flare with very important implications for blazar modelling. All multi-messenger diagnostics reported here support a single coherent picture in which TXS 0506+056, a very high energy  $\gamma$ -ray blazar, is the only counterpart of all the neutrino emissions in the region and therefore the most plausible first non-stellar neutrino and, hence, cosmic ray source.



### 3 Publications-2017

- R. Ruffini,M. Karlica, N. Sahakyan, J. Rueda, Y. Wang, G. Mathews, C. Bianco, M. Muccino, "A GRB Afterglow Model Consistent with Hypernova Observations", *The Astrophysical Journal*, Volume 869, Issue 2, article id. 101, 9 pp. 2018.
- A. Abeysekara, ... N. Sahakyan, ... D. Zaric, "Periastron Observations of TeV Gamma-Ray Emission from a Binary System with a 50-year Period", *The Astrophysical Journal Letters*, Volume 867, Issue 1, article id. L19, 8 pp., 2018.
- N. Sahakyan and S. Gasparyan "Dissecting the region around IceCube-170922A: the blazar TXS 0506+056 as the first cosmic neutrino source", *Monthly Notices of the Royal Astronomical Society*, Volume 480, Issue 1, p.192-203, 2018.
- N. Sahakyan, "Lepto-hadronic  $\gamma$ -Ray and Neutrino Emission from the Jet of TXS 0506+056", *The Astrophysical Journal*, Volume 866, Issue 2, article id. 109, 6 pp. 2018.
- S. Gasparyan, N. Sahakyan, V. Baghmanyian, D. Zargaryan, "On the Multiwavelength Emission from CTA 102", *The Astrophysical Journal*, Volume 863, Issue 2, article id. 114, 11 pp., 2018.
- M. Aartsen, .... N. Sahakyan, .... T. Yuan, "Neutrino emission from the direction of the blazar TXS 0506+056 prior to the IceCube-170922A alert", *Science*, Volume 361, Issue 6398, pp. 147-151, 2018.
- V. Baghmanyian, M. Tumanyan, N. Sahakyan, Y. Vardanyan, "High-Energy  $\gamma$  -Ray Emission from PKS 0625-35", *Astrophysics*, Volume 61, Issue 2, pp.160-170, 2018.
- N. Sahakyan, V. Baghmanyian, D. Zargaryan, "Fermi-LAT observation of nonblazar AGNs", *Astronomy & Astrophysics*, Volume 614, id.A6, 11 pp., 2018.

- B. Fraga, U. Barres de Almeida, S. Gasparyan, P. Giommi, N. Sahakyan, "Time-Evolving SED of MKN421: a multi-band view and polarimetric signatures", *Frontiers in Astronomy and Space Sciences*, Volume 5, id.1, 2018.
- S. Gasparyan, N. Sahakyan, P. Chardonnet, "The origin of HE and VHE gamma-ray flares from FSRQs", *International Journal of Modern Physics D*, Volume 27, Issue 10, id. 1844007, 2018.
- D. Zargaryan, N. Sahakyan, H. Harutyunian, "Chandra observations of gamma-ray emitting radio galaxies", *International Journal of Modern Physics D*, Volume 27, Issue 10, id. 1844022, 2018.
- V. Baghmanyan, N. Sahakyan, "X-ray and  $\gamma$ -ray emissions from NLSy1 galaxies", *International Journal of Modern Physics D*, Volume 27, Issue 10, id. 1844001, 2018.

### **3.1 Publications-2012-2017**

- D. Zargaryan, S. Gasparyan, V. Baghmanyan and N. Sahakyan, "Comparing 3C 120 jet emission at small and large scales", *Astronomy & Astrophysics*, Volume 608, id. A37, 10, 2017.
- U. Barres de Almeida, F. Bernardo, P. Giommi, N. Sahakyan, S. Gasparyan and C. Brandt, "Long-Term Multi-Band and Polarimetric View of Mkn 421: Motivations for an Integrated Open-Data Platform for Blazar Optical Polarimetry", *Galaxies*, vol. 5, issue 4, p. 90, 2017.
- V. Baghmanyan, S. Gasparyan and N. Sahakyan, "Rapid Gamma-Ray Variability of NGC 1275", *The Astrophysical Journal*, Volume 848, Issue 2, article id. 111, 8, 2017.
- N. Sahakyan and S. Gasparyan "High energy gamma-ray emission from PKS 1441+25", *Monthly Notices of the Royal Astronomical Society*, 470, 3, p.2861-2869, 2017.
- N. Sahakyan, V. Baghmanyan, and D. Zargaryan, "Gamma-ray Emission from Non-Blazar AGNs", *AIP Conference Proceedings*, Volume 1792, Issue 1, id.050002, 2017.

- N. Sahakyan and S. Gasparyan, "High Energy Gamma-Rays From PKS 1441+25", AIP Conference Proceedings, Volume 1792, Issue 1, id.050005, 2017.
- V. Baghmanyan, "Gamma-Ray Variability of NGC 1275", AIP Conference Proceedings, Volume 1792, Issue 1, id.050007, 2017.
- D. Zargaryan, "The Gamma-Ray Emission from Broad-Line Radio Galaxy 3C 120", AIP Conference Proceedings, Volume 1792, Issue 1, id.050008, 2017.
- N. Sahakyan, "Galactic sources of high energy neutrinos: Expectation from gamma-ray data", EPJ Web of Conferences, Volume 121, id.05005, 2016.
- Sahakyan, N., Zargaryan, D. and Baghmanyan, V. "On the gamma-ray emission from 3C 120", Astronomy & Astrophysics, Volume 574, id.A88, 5 pp., 2015.
- Sahakyan, N., Yang, R., Rieger, F., Aharonian, F. and de Ona-Wilhelmi, E. "High Energy Gamma Rays from Centaurus a" Proceedings of the MG13 Meeting on General Relativity ISBN 9789814623995, pp. 1028-1030, 2015.
- Sahakyan, N., Piano, G. and Tavani, M. "Hadronic Gamma-Ray and Neutrino Emission from Cygnus X-3", The Astrophysical Journal, Volume 780, Issue 1, article id. 29, 2014.
- Sahakyan, N., Rieger, F., Aharonian, F., Yang, R., and de Ona-Wilhelmi, E. "On the gamma-ray emission from the core and radio lobes of the radio galaxy Centaurus A", International Journal of Modern Physics: Conference Series, Volume 28, id. 1460182, 2014.
- Sahakyan, N., Yang, R. Aharonian, F. and Rieger, F., " Evidence for a Second Component in the High-energy Core Emission from Centaurus A?", The Astrophysical Journal Letters, Volume 770, Issue 1, L6, 2013.
- Yang, R.-Z., Sahakyan, N., de Ona Wilhelmi, E., Aharonian, F. and Rieger, F., "Deep observation of the giant radio lobes of Centaurus A with the Fermi Large Area Telescope", Astronomy & Astrophysics, 542, A19, 2012.

### *3 Publications-2017*

---

- Sahakyan, N., "High energy gamma-radiation from the core of radio galaxy Centaurus A", *Astrophysics*, 55, 14, 2012.
- Sahakyan, N., "On the Origin of High Energy Gamma-Rays from Giant Radio Lobes Centarus A", *International Journal of Modern Physics Conference Series*, 12, 224, 2012.

# 4 Lepto-hadronic $\gamma$ -ray and neutrino emission from the jet of TXS 0506+056

## 4.1 Introduction

Recently, IceCube detected Very High Energy (VHE;  $> 100$  GeV) neutrinos from extragalactic sources [3, 33], [4]. This opens new perspectives for investigation of nonthermal processes in astrophysical objects even though no sources emitting these neutrinos have been identified so far. As neutrinos are not absorbed when interacting either with a photon field or the matter, unlike the  $\gamma$ -rays, they can be detected from distant sources which are "Terra Incognita" for  $\gamma$ -ray observations.

Different types of objects are proposed as potential sources for VHE neutrino emission among which the most prominent are Active Galactic Nuclei (AGNs). AGNs, being powered by supermassive black holes, are among the most luminous and energetic extragalactic objects. When the jet of an AGN is aligned with an observer's line of sight, they appear as blazars [142] which, based on the observed emission lines, are commonly sub-divided into BL Lacertae (BL-Lac) objects and Flat-Spectrum Radio Quasars (FSRQs). Blazars are characterized by high luminosity (e.g.,  $10^{48} - 10^{49}$   $erg\ s^{-1}$  in the  $\gamma$ -ray band) and variable nonthermal emission in the radio to the VHE  $\gamma$ -ray bands. As blazar emission is dominating in the extragalactic  $\gamma$ -ray sky, it is natural to consider them as the most probable sources of the observed neutrinos. In fact, Padovani & Resconi [51], Padovani et al. [52], have recently found a correlation between High Energy (HE) peaked BL Lacs (emitting  $> 50$  GeV) detected by Fermi Large Area Telescope (Fermi-LAT) and the VHE neutrino sample detected by IceCube. Also, remarkable is the possible association of the highest-reconstructed-energy ( $\sim 2$  PeV) neutrino event with the exceptionally bright phase of FSRQ PKS B1414-418 [37]. Recently, Aartsen et al. [2]

showed that the maximum contribution of the known blazars to the observed astrophysical neutrino flux in the energy range between 10 TeV and 2 PeV is less than 27 %, but in principle significant neutrino emission from a particularly bright blazar can be detected.

There are proposed different mechanisms for VHE neutrino production in blazar jets (e.g., Mannheim [43], Bednarek [15], Protheroe [56], Yoshida et al. [66], Tavecchio & Ghisellini [63], [48, 65, 42]). These relativistic jets are ideal laboratories where the leptons (electrons) and hadrons (protons) can be effectively accelerated, which interacting with the magnetic and/or photon fields can produce emission across the whole electromagnetic spectrum. Even if the leptonic emission alone can explain the observed features of some blazars, the energetic protons co-accelerated with electrons might contribute to the observed emission. As the protons probably carry a significant fraction of the total jet power, the exact estimation of their content in the jet is crucial for understanding the jet launching, collimation and dynamics. In general, only HE  $\gamma$ -ray observations alone are not sufficient to differentiate between the contribution of protons and electrons; this can be done only by neutrino observations.

The lack of a high-confidence association of a neutrino event with a particular blazar significantly complicates the interpretation of hadronic emission from blazar jets. The best association to date is that between IceCube-170922A neutrino event with the  $\gamma$ -ray bright BL Lac object TXS 0506+056 [32]. The Fermi LAT and MAGIC observations reveal that TXS 0506+056 was in the active state in MeV/GeV and above 100 GeV bands when the neutrino event was observed on September 22, 2017; the evolution of its multiwavelength emission in time around the neutrino event can be seen here [youtu.be/1FBciGIT0mE](https://youtu.be/1FBciGIT0mE) [50]. At the redshift of  $z = 0.336$  [53] TXS 0506+056 is among the brightest BL Lacs detected by Fermi LAT. Moreover, IceCube detected a  $3.5\sigma$  excess of neutrinos from the direction of TXS 0506+056 in 2014-2015 [34]. Further detailed spatial and temporal analyses of the complex  $\gamma$ -ray region around TXS 0506+056 showed that the emission from the nearby flaring blazar PKS 0502+049 is dominating at low energies, but TXS 0506+056 is brighter above a few GeV, making it the most probable neutrino source [50].

The data available from the observations of TXS 0506+056 makes it a unique object for testing the lepto-hadronic emission scenarios in blazar jets. For example, in Ahnen et al. [8] the one-zone lepto-hadronic model based on the interaction of both accelerated electrons and protons (photo-meson reaction)

with the external photons (from a slow-moving external layer) can successfully explain the observed multiwavelength SED and neutrino rate if the proton energies are in the range from  $10^{14}$  eV to  $10^{18}$  eV. In this and other similar models it is impossible to estimate the relative contribution of low-energy protons ( $> 1$  GeV) which carry a significant portion of the jet power. An alternative modeling of the multiwavelength emission from TXS 0506+056 is applied in the current paper; it is assumed that the protons accelerated in the jet of TXS 0506+056 interact with a dense target crossing the jet and produce the observed HE and VHE  $\gamma$ -ray emission from the decay of neutral pions. This is done within widely discussed jet-target interaction models which were successfully applied for modeling the emission from different AGNs (e.g., M87 [12, 13], Cen A core [9], Mrk 421 [23], 3C454.3 [41], etc.). The initial proton distribution is estimated by normalizing the expected  $\gamma$ -ray flux from proton-proton ( $pp$ ) interactions to the Fermi LAT and MAGIC data, then the neutrino spectra are estimated straightforwardly. There is no contradiction between this and other discussed models involving photo-meson reactions as, again, the cascade initiated from the interaction of ultrahigh-energy protons might be still responsible for the emission in the X-ray band. By interpreting that the observed HE and VHE  $\gamma$ -ray emission originates from  $pp$  interactions, the main purpose of the current paper is to estimate i) the total luminosity of protons ( $>$  GeV) and compare it with that of electrons and ii) the expected detection rate of neutrinos produced from  $pp$  inelastic collisions.

The paper is structured as follows: the model adopted here is described in Section 5.2. The modeling of broadband emission from TXS 0506+056 is presented in Section 5.3. The results are discussed in Section 5.4 and summarized in Section 5.5.

## 4.2 Broadband emission from jets

Dominantly, the emission from blazars is of a non-thermal nature, extending from radio to VHE  $\gamma$ -ray bands, with two broad humps in the spectral energy distribution (SED), peaking in the IR-X-ray and MeV-TeV bands. This double-peaked feature can be attributed to radiative losses of non-thermal electrons. The low-energy component can be well explained by synchrotron emission of relativistic electrons in the jet and the inverse Compton scattering of soft target photons on these electrons can be responsible for the HE peak.

The target photon fields depend mostly on the location of the emission region [140], being of different origin and varying along the jet. For example, for BL Lacs with very weak (or absent) emission lines, the target photons can be synchrotron photons (synchrotron self Compton (SSC) [103, 115, 85]), whereas for FSRQs where the jet propagates in an environment reach of photons, the HE component can originate also from inverse Compton scattering of external photons (e.g., photons reflected from Broad Line Region (BLR) [139] or from a dusty torus [84, 104]). These models have been successful in explaining several features observed in the non-thermal spectra of blazars, e.g., spectra in different bands, simultaneous or non-simultaneous flux increases (decreases), etc. However, the observation of minute-scale  $\gamma$ -ray variability of blazars poses severe difficulties for one-zone leptonic scenarios; the emission region will be beyond the event horizon of the central black holes only in case of extremely high bulk Lorentz factors (e.g., see [11, 6]). Therefore, there have been proposed more complex scenarios: multi-zone models (e.g., spine-sheath [62], decelerating-jet [26], jets in a jet [30, 31], etc.) and internal-shock models (e.g., [46, 61, 60, 36, 22]).

The HE component in blazar SEDs can be also explained by applying alternative models invoking the radiative output of hadrons accelerated in the jets of blazars. The protons unavoidably accelerated in jets can interact with matter (proton-proton [ $pp$ ]), magnetic or radiation field (proton- $\gamma$ ) and produce the observed HE emission. In the last two cases, in order to emit either through proton-synchrotron emission [5, 47] or photo-pion production [44], the protons should be accelerated to extremely high energies ( $E_p \geq 10^{19}$ eV) and propagate in a highly magnetized plasma ( $B \geq 30$  G). These requirements for the protons and/or the medium can be somewhat softened when a highly collimated proton beam accelerated in the jet penetrates into a dense and compact target (e. g., cloud(s) from BLR Dar & Laor [23], Beall & Bednarek [14], Araudo et al. [9]) and produces the observed HE  $\gamma$ -rays through inelastic  $pp$  scattering. In addition, at larger distances from the nucleus rich in star populations, the star-jet interactions too can produce HE  $\gamma$ -rays [12, 10, 14, 17, 16, 24]. In these cases, the protons should be accelerated only up to moderate  $\simeq 100$  TeV energies unlike the other models.

### 4.2.1 The model

The interaction of the blazar jets with clouds or stars abundant in their environment does not significantly affect the dynamics of the jet and its propagation to  $kpc$  scales, but it provides targets for efficient hadronic interactions. The strong shock formed at interaction of relativistic flows with dense targets can accelerate the particles and in some cases their interactions can be responsible for the steady (e.g., several clouds can interact with the jet simultaneously) or flare-like  $\gamma$ -ray emissions. The studies of hydrodynamical simulations of jet-target interactions and dynamical time scales required for particle acceleration and emission show that star-target interactions can produce detectable  $\gamma$ -ray fluxes not only in the nearby (e.g., Cen A [9] and M87 [12]) but also in distant/powerful objects (e.g., 3C 454 [41], Mrk 421 [14, 23]). For a comprehensive and detailed study of the hydrodynamical simulation of jet-cloud/star interactions and discussion of jet stability see Bosch-Ramon et al. [21] and Perucho et al. [54].

The scenarios mentioned above require several parameters for accurate estimation of the duration, rate and efficiency of interactions and the related radiative outputs. The parameters describing the targets (e.g., clouds or stars envelopes) and the energy distribution of accelerated protons are different for each source, but even within the typical values (e.g., clouds with  $\sim 10^{10} - 10^{12} \text{ cm}^{-3}$  density and  $\sim 10^{12} - 10^{13} \text{ cm}$  radius) the powerful jet-target interactions can produce observable  $\gamma$ -ray emission. Another important parameter is the distance ( $d$ ) from the base of the jet where the interaction occurs. Star-jet/cloud interaction cannot occur within the jet formation region and also at large distances from the central source, as the jet energy flux decreases with the distance as  $F_j \simeq L_j / \pi \theta^2 d^2$  ( $\theta$  is the jet opening angle). For very powerful jets the jet energy flux might be still high enough for an effective interaction farther from the jet launching point which will also allow the protons to be accelerated to HEs. On the other hand, for low-power jets, when the penetration occurs in the innermost part of the jet, the protons can be further accelerated in the target, gaining energies required for HE  $\gamma$ -ray emission [9, 12]. Even though the jet-target interactions can occur frequently, for some jets the observed  $\gamma$ -ray emission is likely to be dominated by boosted SSC emission from jet-accelerated electrons. However, in some cases when the leptons cool faster not reaching HEs or due to some internal changes in the jet affecting only the boosted emission, the hadronic component produced in star-jet interactions can dominate and produce the observed HE and VHE  $\gamma$ -

rays . Such scenario can be applied only when  $\gamma$ -ray and neutrino emissions are detected, e.g., from TXS 0506+056.

Since our primary goal is to investigate whether the observed HE and VHE  $\gamma$ -ray and neutrino emission from TXS 0506+056 can be explained by the interaction of moderately accelerated protons and measure their content in the jet, here, without going much in details (e.g., the nature of target, at which distance the interaction occurred, etc.), the broadband SED of TXS 0506+056 obtained during the neutrino event detection is modeled. Assuming that the energetic protons (either accelerated in the jet or in the target) interact in a target with a typical density of  $10^{10} \text{ cm}^{-3}$ , the  $\gamma$ -rays are produced through  $pp$  interactions. Most likely, the maximum energy of protons will be defined by the size of acceleration region rather than by radiative losses, i.e. at a rate close to the theoretical limit  $t_{acc} \sim R/c$ . Expressing the acceleration time as  $E/dE/dt$ , where  $dE/dt \simeq \eta eBc$  [7] is the proton acceleration rate with  $\eta$  efficiency, implies that  $E_{max} \simeq 3.0 \times 10^{15} (\eta/0.1) (B/1G) (R/10^{13} \text{ cm})$  eV. So, even if the proton acceleration occurs in a relatively small ( $\sim 10^{13}$  cm) dense target,  $E$  goes well beyond  $\sim 10$  PeV, enough to produce the observed VHE  $\gamma$ -ray photons and neutrino. In the case when the protons are accelerated in the jet, in the frame of the target their energy will be even higher due to Doppler boosting. The protons interacting in the target produce  $\gamma$ -rays from the decay of neutral pions ( $\pi^0 \rightarrow \gamma\gamma$ ), while the neutrinos ( $\nu_\mu, \nu_e$ ) are produced from the decay of  $\pi^\pm$  (e.g.,  $\pi^+ \rightarrow \mu^+ + \nu_\mu \rightarrow e^+ + \nu_e + \nu_\mu + \bar{\nu}_\mu$ ). The observed  $\gamma$ -ray luminosity of TXS 0506+056 around 10 GeV (most likely the peak of HE component) is  $\simeq 4 \times 10^{46} \text{ erg s}^{-1}$ , then assuming the efficiency of energy transfer from relativistic protons to secondary particles is  $\sim 10\%$ , the required proton luminosity should be  $L_p \simeq 4 \times 10^{47} \text{ erg s}^{-1}$ . Next, assuming the proton acceleration efficiency is roughly 10%, the jet power would be  $L_{jet} \simeq 4 \times 10^{48} \text{ erg s}^{-1}$  - a value usually estimated for bright blazars. Thus, both the maximum energy of protons and the required luminosity are physically realistic and the observed HE and VHE  $\gamma$ -ray emission from TXS 0506+056 can be due to  $pp$  interactions.

### 4.3 SED modeling

The broadband SEDs of TXS 0506+056 for low (period 1 [P1]) and high (period 2 [P2]) VHE  $\gamma$ -ray emitting states (when the neutrino was detected) are shown in Fig. 4.1 (taken from [8]). As compared with the archival data (light

gray), i) the low energy component is relatively constant and ii) the HE component slightly increases and the spectrum extends above several hundreds of GeV. This well fits in the scenario discussed above; the synchrotron emission of electrons accelerated in the jet is almost unchanged while most likely a different process is responsible for the HE emission in the active states. It is natural also to expect that the  $\gamma$ -ray flux produced by the same electrons remains the same as the time-averaged one.

The emissions from two different jet regions are considered in the SED modeling: i) the observed low-energy and time-averaged HE components are explained as emission directly from jet-accelerated electrons in a compact region moving with the bulk Lorentz factor of the jet and ii) during the active  $\gamma$ -ray emitting state, when the neutrino was observed, the  $\gamma$ -rays are produced from the inelastic  $pp$  interactions in the second emission site. Such a compact emitting region is usually considered when modeling the multi-wavelength emission from blazars (e.g., [103, 115, 85]), while the second zone is expected to form when a target penetrates into the jet (see the sketch in Fig. 1 of [21] where a jet-target interaction is illustrated). Next, the emission from the  $e^-e^+$  pairs produced from the decay of charged pions in the target, which can be significant in the X-ray band, is also taken into account. This modeling allows to estimate both the electron and proton content in the jet.

The radiative contribution of electrons is computed within the one-zone scenario, assuming the emission region (the "blob") is a sphere with a radius of  $R$  moving with a bulk Lorentz factor of  $\Gamma$ , carrying a magnetic field of  $B$  and having a population of relativistic electrons with an energy distribution of

$$N'_e(E'_e) \sim E'^\alpha_e \exp\left(-\frac{E'_e}{E'_{cut}}\right) \quad (4.3.1)$$

between  $E'_{min}$  and  $E'_{max}$  [35];  $E'_{cut}$  is the cut-off energy. As the contemporaneous data from the rising part of the low energy component are missing, the electron spectral index  $\alpha$  can not be measured, so  $\alpha = 2$  expected from acceleration theories is used. Also,  $E'_{min} = 100$  MeV is used, so the model does not overpredict the archival radio data. The luminosity of the synchrotron emission of these electrons will be amplified by a relativistic Doppler factor of  $\delta$  ( $\delta = \Gamma$  for small jet viewing angles), for which  $\delta = 25$  was used, a characteristic value for bright blazars [105]. The observations of TXS 0506+056 in the X-ray, HE and VHE  $\gamma$ -ray bands allowed to infer a variability time scale of  $t_d \leq 10^5$  s (e.g., [39, 8] which implies that the emission is produced in sub-

parsec regions of the jet, so  $R \simeq 7.5 \times 10^{16}$  cm will be used.

The energy distribution of protons accelerated in the jet can be also expressed as

$$N_p(E_p) \sim E_p^{-\alpha_p} \exp\left(-\frac{E_p}{E_{c,p}}\right) \quad (4.3.2)$$

where  $E_{c,p}$  is first considered as a free parameter then  $E_{c,p} = 10$  PeV is used as the  $\gamma$ -ray data there is no sign of any spectral cutoff.  $\gamma$ -rays, neutrinos and  $e^-e^+$  pairs will be produced in the interactions of these protons. The characteristic cooling time of  $pp$  collisions is  $t_{pp} \simeq (K\sigma_{pp}n_H)^{-1} \simeq 10^{15}/n_H$  which is inversely proportional to the target particle number density. In case of optimal radiation  $t_{pp} \simeq t_v$  ( $t_v = 10^5$  s) the target density is  $n_H = 10^{10} \text{ cm}^{-3}$ . The size of the emitting target can be estimated as  $r = (3M_c t_v / 4 \pi 10^{15} m_p)^{1/3} \simeq 5.2 \times 10^{13} (M_c / 10^{28} \text{ g})^{1/3} \text{ cm}$  (e.g., from Barkov et al. [12] for the weak tidal disruption). We note that this number density and size are typically estimated for the clouds in BLR (e.g., [49, 55]) and adopted in star-cloud (e.g., Araudo et al. [9]) or star-jet (e.g. Barkov et al. [12]) scenarios. As the target density is high, the protons lose a significant fraction of their energy at  $pp$  collisions: the interaction is in a radiatively efficient regime,  $t_{pp} \leq t_v$ , so most of the  $\gamma$ -rays are emitted around  $t_v$  rather than when the target is already accelerated to high velocities. The  $\gamma$ -ray and neutrino spectra above 100 GeV are calculated using the analytic approximations from Kelner et al. [40], while the delta function approximation for lower energies is used (for exact formula see Sahakyan et al. [57]). The secondary  $e^-e^+$  pairs spectrum will be similar to that of  $\gamma$ -rays but shifted to lower energies (see Eq. 62 in Kelner et al. [40]).

During the fitting (synchrotron/SSC emission of jet-accelerated electrons and  $pp$  interactions) the model free parameters are derived by Markov Monte Carlo Chain sampling of their likelihood distributions [146]. This allows to obtain the parameters and their uncertainties which best describe the observed spectra statistically. The following expected ranges are considered:  $1.5 \leq \alpha_p \leq 10$ ,  $0.511 \text{ MeV} \leq E'_{cut}$ ,  $E_{c,p} \leq 10 \text{ TeV}$ , and the normalization of electrons/protons and  $B$  are defined as positive parameters.

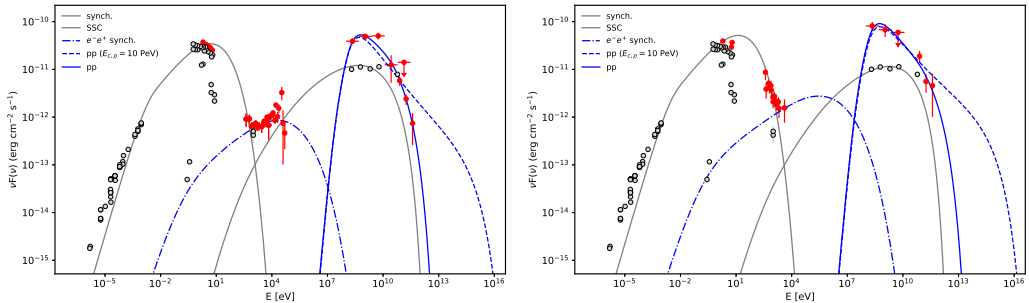


Figure 4.1 The broadband SED of TXS 0506+056 for the active (left) and low VHE  $\gamma$ -ray emitting states. The boosted synchrotron/SSC emission from the jet are shown in gray whereas the  $\gamma$ -ray spectra from pp interactions and synchrotron emission from secondary  $e^-e^+$  pairs are shown with blue color. The data are corrected for EBL absorption adopting the model from Domínguez et al. [25].

## 4.4 Results and Discussions

Detailed temporal and spatial analyses of the complex  $\gamma$ -ray region around the VHE neutrino event IceCube-170922A illustrates that most likely TXS 0506+056 is the source of the observed VHE neutrinos [50]. This is a direct evidence that cosmic rays (protons) are effectively accelerated in the jet of TXS 0506+056. The data available from the multiwavelength observations of TXS 0506+056 around the neutrino event make this source an interesting (unique) object where the HE and VHE processes can be investigated using  $\gamma$ -rays as well as neutrinos.

The multiwavelegth SEDs modeled within the combined leptonic/hadronic scenario are shown in Fig. 4.1. The boosted synchrotron emission from the jet-accelerated electrons can explain the low-energy component, while the SSC radiation of the same electrons- the time averaged  $\gamma$ -ray data (solid gray line in Fig. 4.1). During P2, the X-ray photon index measured by Swift XRT is relatively steep ( $\Gamma_X > 2.5$ ), corresponding to the HE tail of synchrotron emission (gray line in the right panel of Fig. 4.1) allowing to estimate the cutoff energy at  $E_c = 8.90 \pm 0.22$  GeV. The magnetic field energy density is  $U_B = 0.88 \times 10^{-3} \text{ erg cm}^{-3}$  (for  $B = 0.15 \pm 0.004$  G) being of the same order as that of the electrons,  $U_e = 1.37 \times 10^{-3} \text{ erg cm}^{-3}$ , meaning the system is close to equipartition. During P1, the X-ray flux that most like is produced by

a different component, limits the cutoff energy at  $6.65 \pm 0.21$  GeV and magnetic field to  $B = 0.10 \pm 0.002$  G, otherwise the model predicted flux will exceed the observed data. The total jet power in the form of magnetic field and electron kinetic energy calculated as  $L_{jet} = \pi c R_b^2 \Gamma^2 (U_B + U_e)$  changes in the range of  $L_{jet} = (7.47 - 9.89) \times 10^{44}$  erg s $^{-1}$ .

The  $\gamma$ -rays produced from the decay of  $\pi^0$  is shown with blue solid and dashed lines in Fig. 4.1. In this case, the slope of proton distribution,  $\alpha_p = 2.41 \pm 0.11$  and  $\alpha_p = 2.49 \pm 0.07$  for P1 and P2, respectively, is directly measured from the  $\gamma$ -ray spectra. As the slopes are relatively steep ( $\alpha_p \simeq 2.5$ ) most of the proton energy output is at lower energies, so the  $\gamma$ -ray emission in the GeV band is mostly dominated by the decay of  $\pi^0$  with no or a negligible contribution from  $e^- e^+$  pairs from  $\pi^\pm$  decay or  $\gamma\gamma$  absorption. When the cut-off energy in Eq. 4.3.2 is taken as a free parameter, it is constrained by the last point in the  $\gamma$ -ray data (with large statistical uncertainty) and corresponds to  $E_{c,p} = 0.98^{+1.68}_{-0.37}$  TeV and  $E_{c,p} = 4.87 \pm 2.93$  TeV, for P1 and P2 respectively. When  $E_{c,p} = 10$  PeV is considered (blue dashed line in Fig. 4.1), the data can be reproduced when  $\alpha_p = 2.54 \pm 0.04$  and  $\alpha_p = 2.46 \pm 0.09$  for P1 and P2, respectively. This modeling predicts emission also beyond the MAGIC data which can not be tested with the current instruments but certainly it is in agreement with the 100 MeV-400 GeV data. The cut-off energy  $E_{c,p} = 10$  PeV is an arbitrary value to show that when higher proton energies are considered the data can be reproduced, but cutoff at much higher energies cannot be excluded.

The modeling of the observed HE and VHE  $\gamma$ -ray data by  $pp$  interactions allows to estimate the total energy of jet protons - perhaps a large fraction of the total jet power. The data can be reproduced when the total proton energy is  $\int E_p N_p(E_p) dE_p \simeq (0.97 - 2.03) \times 10^{53}$  erg corresponding to maximum luminosity of  $L_p = W_{pp}/t_{pp} \simeq 2.0 \times 10^{48}$  erg s $^{-1}$ . In this case we note that for the cloud size of  $5.2 \times 10^{13}$  cm and a number of density of  $10^{10}$  cm $^{-3}$ , the total energy of target protons is only a small fraction ( $\sim 10^{-5}$ ) of that of jet protons.  $W_{pp}$  strongly depends on  $n$  which is unknown and in this case is roughly constrained by the observed flux variation. However, even if it will differ from the used value by two orders of magnitude, the jet luminosity would be still realistic as it is measured in the rest frame. For example, the other hadronic models involving photo-meson interactions the required proton luminosity is much higher (e.g.,  $L_p \simeq 10^{49}$  erg s $^{-1}$ ). The proton luminosity exceeds the power carried by the electrons  $\sim 10^3$  times, making a significant contribution

to the jet kinetic luminosity. Interestingly, this is similar to the difference between electron and proton luminosities usually estimated assuming one proton per electron. Clearly, both the predicted spectral shapes and the required total energy are physically reasonable, meaning that the  $pp$  interactions can solely contribute to the observed HE and VHE  $\gamma$ -rays.

If the  $\gamma$ -rays observed from TXS 0506+056 are due to the interaction of protons in the target crossing the jet, secondary  $e^-e^+$  pairs will be also produced whose emission can be significant in the X- or  $\gamma$ -ray bands. As in the target the magnetic field most likely exceeds that in the jet, e.g., due to higher density of particles, these pairs dominantly will lose energy by synchrotron radiation (a sketch of a jet target interaction scenario can be seen in Fig. 1 of [21]). In this case, the bremsstrahlung energy losses with a cooling time of  $t_{br} \simeq 10^{16}/(\ln(E_e/m_ec^2) + 0.26)$  s [18] in a completely ionized medium is significantly longer than that of synchrotron emission (for  $B \geq 1$  G). The estimation of the magnetic field in the target is a rather difficult task, depending on the nature of the target, whether it is a cloud or a star envelope. This magnetic field is not necessarily constant, e.g., it can decrease due to expansion of the cloud or increase due to the continuous pumping of jet energy. Possible emission mechanisms when the cloud penetrates into the jet of M87 are discussed in [13]. The blue dot-dashed line in Fig. 4.1 shows the synchrotron emission of secondary  $e^-e^+$  pairs in  $\sim 80$  G magnetic field. At lower energies, the boosted synchrotron emission of electrons directly accelerated in the jet is dominating but due to continuous electron energy losses by synchrotron and SSC radiations, this emission quickly drops already in the X-ray band. Being more energetic, the synchrotron emission from fresh  $e^-e^+$  pairs can dominate beyond the X-ray band, reaching HEs. The synchrotron emission of  $e^-e^+$  pairs i) can relatively well explain the X-ray spectrum observed during P1 when  $B = 80$  G (left panel in Fig. 4.1) and ii) for the magnetic field  $\sim 800$  times stronger than that in the jet, it does not overproduce the data detected by Swift XRT during P2 (right panel in Fig. 4.1) which are most likely due to synchrotron emission of jet electrons. It is interesting that the proton energy required to explain the observed HE and VHE  $\gamma$ -ray data is also sufficient for transferring enough energy to secondary electrons, so their synchrotron emission can explain the observed X-ray data for a reasonable magnetic field. This strengthens the used hadronic model. However, this X-ray emission in principle might arise also from the synchrotron emission of the secondary pairs produced in the cascades initiated by ultrahigh-energy protons [8].

Having calculated the luminosity of protons and their energy distribution, the spectra of HE neutrinos can be calculated straightforwardly and a limit on the expected number of events detectable by IceCube from TXS 0506+056 in a certain exposure time ( $t_{exp}$ ) can be obtained. The neutrinos produced from the protons with an energy distribution of Eq. 4.3.2 will have a spectrum of  $\sim E_\nu^{-\alpha_\nu} \exp(-\sqrt{E_\nu/E_{\nu,c}})$  where  $\alpha_\nu \simeq \alpha_p - 0.1$  and  $E_{\nu,c} \simeq E_{c,p}/40$  [38]. Therefore, even when  $E_{c,p} = 10$  PeV in the spectrum of neutrinos the cutoff is at  $E_{\nu,c} \simeq 250$  TeV, close to the energy of the observed IceCube-170922A event. Next, using the effective area ( $A_{eff}(E_\nu)$ ) most sensitive for the location of TXS 0506+056 from Aartsen et al. [1], the number of expected events can be estimated as  $N_\nu \simeq t_{exp} \int A_{eff}(E_\nu) \Phi_\nu(E_\nu) dE_\nu$ . This effective area reaches its optimal (maximum) value for neutrino energies above several hundreds of TeV, so to estimate the expected neutrino rates, a significant impact will have the interactions of protons with  $E_p \geq 1$  PeV. The number of expected events is proportional to the duration of the active emission phase of the source. The  $\gamma$ -ray light curve of TXS 0506+056 calculated above 2 GeV to avoid any bias from the nearby PKS 0502+049 is shown in Fig. 5 of [50]. As one can see the source was in its active phase around the IceCube-170922A event at least for  $t_{exp} > 200$  days. Indeed, the  $\gamma$ -ray observations suggest that the active period can be  $\sim 0.5 - 1$  year [8, 32, 39]. Here we use  $t_{exp} = 60$  days corresponding to the period when VHE  $\gamma$ -rays from TXS 0506+056 were observed and  $t_{exp} = 0.5$  -year corresponding to the most prolonged active/bright state of the source. When  $E_{c,p} = 10$  PeV, the expected rates during P1 and P2 are  $\simeq 0.04$  and  $\simeq 0.15$  respectively for  $t_{exp} = 60$  days, and  $\simeq 0.13$  and  $\simeq 0.46$  respectively for  $t_{exp} = 0.5$  -year. Yet, assuming the proton acceleration continues beyond 10 PeV or the source active phase is longer, the expected rate would be even higher.

## 4.5 Conclusions

In blazar studies, one of the long-standing and unclear questions is whether the protons are effectively accelerated in their jets and if they have a significant contribution to the observed emissions. The  $\gamma$ -ray observations solely are not sufficient to differentiate between the emission from electrons and protons not allowing to estimate their content in jets exactly. The recent association of TXS 0506+056 with the neutrino events allowed to measure the total energy of the jet carried by electrons and protons.

When the observed  $\gamma$ -rays and neutrinos from a blazar are due to  $pp$  interactions, the energy of protons is mostly released in the GeV band allowing straightforward measurement of the proton spectra based on the observed  $\gamma$ -ray data. A simplified scenario of lepto-hadronic emission from TXS 0506+056 is discussed assuming that beside the constant boosted electron synchrotron/SSC emission from the jet compact region, a significant radiation in the  $\gamma$ -ray band is produced when a target (cloud, star envelope, etc.) crosses the jet and the inelastic  $pp$  interactions produce pions which then decay into  $\gamma$ -rays. If only the emission from the leptons is considered, the electrons and magnetic field are in equipartition and the observed low-energy and time-averaged  $\gamma$ -ray data can be explained for the jet luminosity of  $L_{jet} \simeq 10^{45} \text{ erg s}^{-1}$ . The  $\gamma$ -ray data when the neutrino was observed, can be modeled if the protons are distributed as  $\sim E_p^{-2.50}$  and their energy extends up to  $E_{c,p} = 10 \text{ PeV}$ . The expected neutrino rate is  $\simeq 0.13 - 0.46$  during the long active phase of the source and  $\sim 0.04 - 0.15$  events if the activity lasts 60 days. The synchrotron emission of electrons directly accelerated in the jet is significant up to the X-ray band, whereas the synchrotron emission of newly injected fresh pairs (from  $pp$  interactions) in a dense target dominates afterwards explaining the observed X-ray data obtained during the low VHE  $\gamma$ -ray emission state of TXS 0506+056. Within this scenario, the energy content of the protons (above  $> \text{GeV}$ ) in the blazar jet is estimated for the first time: the required proton injection luminosity should be  $\simeq 2.0 \times 10^{48} \text{ erg s}^{-1}$  which exceeds  $10^3$  times that of electrons. This implies that a significant fraction of the jet kinetic energy is carried by the protons but still involvement of hadrons acceleration in the jet will not dramatically (unreasonably) increase its luminosity. Considering the applied model can satisfactorily reproduce the observed multiwavelegh emission spectrum of TXS 0506+056 and predicts a sufficient neutrino production rate, it provides an acceptable explanation for the hadronic emission from the TXS 0506+056 jet.



# 5 On the multi-wavelength Emission from CTA 102

## 5.1 Introduction

The blazars are the most extreme class of radio-loud active galactic nuclei (AGNs) in their unification scheme. Blazars are emitting electromagnetic radiation ranging from radio to High and Very High Energy  $\gamma$ -ray bands (HE;  $\geq 100$  MeV and VHE;  $\geq 100$  GeV) characterized by rapid and high-amplitude variability which can be explained assuming the jets are oriented close to the line of sight of the observer (a few degrees) and the nonthermal plasma moves with relativistic velocities along the jet [142]. Blazars are grouped into two large sub-classes, Flat Spectrum Radio Quasars (FSRQs) and BL Lacertae objects (BL Lacs), on the basis of different emission line properties, which are stronger and quasar-like in FSRQs and weak or absent in BL Lacs. An alternative classification method is based on the luminosity of the broad emission lines (or accretion disc) measured in Eddington units: when  $L_{BLR}/L_{Edd} \geq 5 \times 10^{-4}$  the objects are FSRQs otherwise they are BL Lacs [107, 135].

The multi-wavelength studies have shown that the Spectral Energy Distributions (SEDs) of both types of blazars consist of two broad humps, peaking in the IR-X-ray (low-energy component) and in the MeV-TeV bands (HE-component). The low-energy component is well explained by synchrotron emission from relativistic electrons in the jet, whereas the nature of the HE-component is less well understood as several different emission mechanisms can be responsible for that emission (e.g., see [140]). The simplest explanation scenario is the synchrotron self-Compton (SSC) radiation, where the soft synchrotron photons are inverse-Compton-up-scattered by the same electrons that have produced the synchrotron emission [103, 85, 115]. As FSRQ jets are in an environment with a stronger external radiation field which can be beamed and enhanced in the frame of the jet, the inverse Compton scat-

tering of external photons too can contribute to the observed HE emission [84, 104, 139]. Alternatively, if the protons are efficiently accelerated in the jet (beyond the threshold for pion production), the HE emission can be also explained by the interaction of energetic protons [121, 120].

After the lunch of Fermi Large Area Telescope (*Fermi*) several thousand blazars were detected in the  $\gamma$ -ray band [75] which opens new perspectives for investigation of the broadband emission from them. The observations indirectly show that the  $\gamma$ -rays can be produced either close to or far from the central black hole. As the  $\gamma$ -ray emission regions are very compact, inferred from extreme short time scale variabilities (e.g., in minute scales [76, 101, 100, 122, 87, 131, 134, 109]) and that there is a sharp break in the GeV  $\gamma$ -ray spectra of some blazars [128], the emission is most likely produced within the broad-line regions (BLRs). On the other hand, the recent detection of  $\geq 100$  GeV photons from several FSRQs [78, 79, 80, 133] implies that the  $\gamma$ -ray emission region should most likely be beyond the BLR in order to bypass strong absorption of VHE photons [128, 112]. Unfortunately, the angular resolution of  $\gamma$ -ray instruments is not high enough (and will not be in the near future) to resolve and localize the  $\gamma$ -ray emission regions which makes it difficult to determine the exact origin of  $\gamma$ -ray emission from blazars as the jet dissipation can occur at any distance from the central black hole.

Among the FSRQs detected by *Fermi*, the powerful GeV  $\gamma$ -ray emitter CTA 102,  $z = 1.037$  [137], is flaring frequently, its  $\gamma$ -ray flux sometimes exceeding  $10^{-5}$   $\text{photon s}^{-1} \text{cm}^{-2}$ . CTA 102 is a luminous, well-studied highly polarized quasar [119] having variable optical emission [126]. It has been initially identified by Compton Gamma Ray Observatory mission as a  $\gamma$ -ray emitter (the flux  $> 100$  MeV being  $(2.4 \pm 0.5) \times 10^{-7}$   $\text{photon s}^{-1} \text{cm}^{-2}$ ), and then it is being included in all the point source catalogs of *Fermi* [74]. Since 2016, CTA 102 was in the enhanced emission state in the UV/optical, X-ray and HE  $\gamma$ -ray bands [90, 82, 94, 127, 95, 88, 96, 83, 118, 89] with several prominent  $\gamma$ -ray bright periods. Considering the available large amount of multi-wavelength data which allows to constrain the emitting region size and location, magnetic field and electron energy distribution, etc., CTA 102 is an ideal object for exploring the physics of FSRQ jets.

In this paper, we analyze the Swift UVOT/XRT, NuSTAR and *Fermi* data collected from 2016 to 2018 to study the broadband emission from CTA 102. The data collected for the analysis and its reduction methods are described in Section 5.2. The spectral changes in different bands during the flaring and low state is discussed in Section 5.3. The broadband SED modeling is presented

in Section 5.4 and Results and Discussion in Section 5.5. The conclusion is summarized in Section 5.6.

## 5.2 Observations and Data Reduction

### 5.2.1 Gamma-ray observations: Fermi LAT

In the present paper we use the publicly available *Fermi* data acquired in the period from 01 January 2016 to 09 January 2018 when large-amplitude flares of CTA 102 were observed. Fermi Science Tools v10r0p5 was used to analyze the data with P8R2\_SOURCE\_V6 instrument response function. Only the 100 MeV - 300 GeV events extracted from a  $12^\circ$  region of interest (ROI) centered on the location of CTA 102 [(RA,dec)= (338.139, 11.720)] have been analyzed. However, the results were checked by repeating the same analyses selecting ROI radii of  $10^\circ$  and  $15^\circ$ . To eliminate the Earth limb events, the recommended quality cuts, (DATA\_QUAL==1)&&(LAT\_CONFIG==1) and a zenith angle cut at  $90^\circ$  were applied. After binning the data into pixels of  $0.1^\circ \times 0.1^\circ$  and into 34 equal logarithmically-spaced energy bins, with the help of gt-like a binned likelihood analysis is performed. The model file describing ROI was created using the *Fermi* third source catalog [74] (3FGL) which contains sources within ROI+ $5^\circ$  from the target, as well as Galactic gll\_iem\_v06 and iso\_P8R2\_SOURCE\_V6\_v06 diffuse components. All point-source spectra were modeled with those given in the catalog, allowing the photon index and normalization of the sources within  $12^\circ$  to be free in the analysis. Also, the normalization of diffuse background components are free. To check if there are new  $\gamma$ -ray sources in the ROI, a Test Statistics (TS) map (TS defined as  $TS = 2(\log L - \log L_0)$ , where  $L$  and  $L_0$  are the likelihoods whether or not the source is included) is created with gttsmap tool which places a point source at each pixel and evaluates its TS. In the TS map, there are new hotspots (pixels) with  $TS > 25$  ( $5\sigma$ ) which possibly hints at the presence of new sources. For each new hotspot we sequentially added a new point source with a power-law spectral definition. For the further analysis the model file containing these additional point sources is used.

In the whole-time analysis, the  $\gamma$ -ray spectrum of CTA 102 was first modeled using a log-parabola [116] as in 3FGL and then assuming a power-law shape. The latter will be used in the light curve calculations, as shorter periods will be considered and a power law can be a good approximation of the

## 5 On the multi-wavelength Emission from CTA 102

---

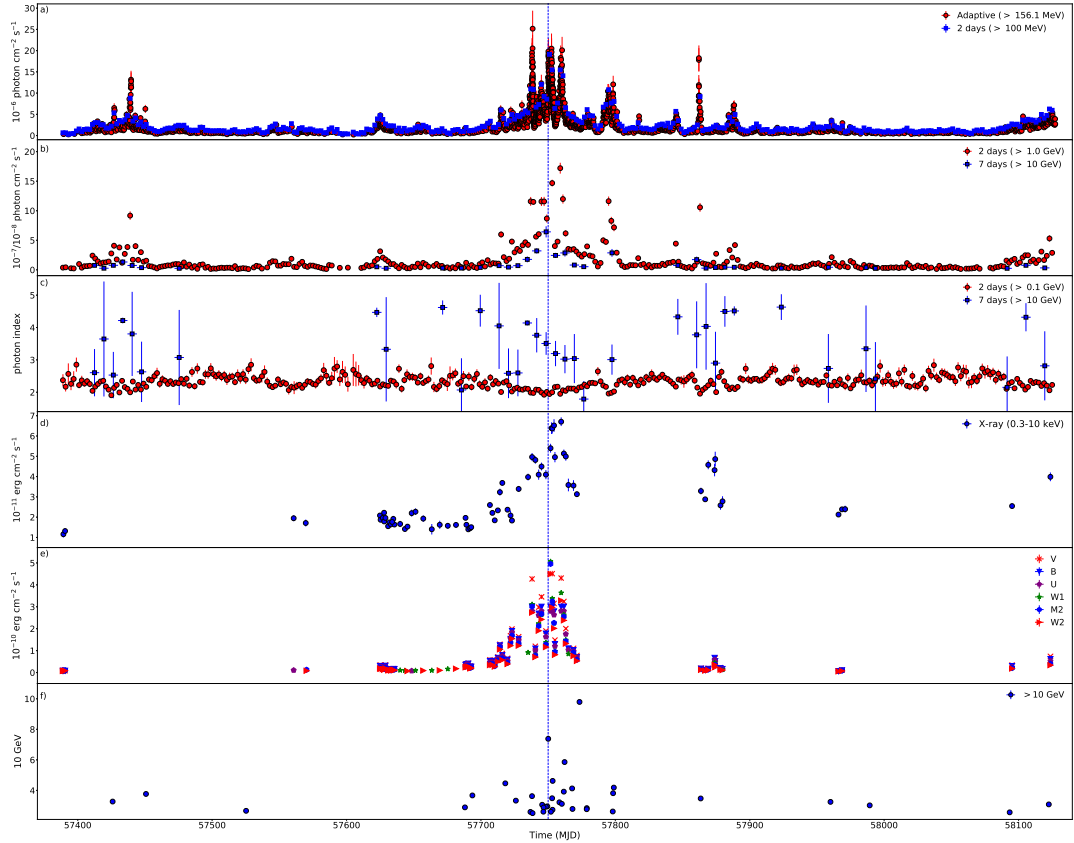


Figure 5.1 Multifrequency light curve of CTA 102 obtained for the period from 2008 August to 2018 January. a)  $\gamma$ -ray light curves with adaptive (red;  $\geq 156.1$  MeV) and 2-day (blue; 100 MeV bins, b) and c) the flux and photon index with 2- and 7-days binning, d) Swift XRT light curve in the 0.3-10 keV range, e) UV/optical fluxes in  $V$ ,  $B$ ,  $U$ ,  $W1$ ,  $M2$  and  $W2$  bands and f) the energy and arrival times of the highest-energy photons. The vertical blue dashed line shows the period when a large flare in the  $R$  – band was observed (28 December 2016).

spectrum. During the analysis of each individual flare a different model file obtained from the analyses of the data accumulated during one/two-month periods covering the flares was also used. An unbinned maximum likelihood analysis was performed using  $(0.1 - 300)$  GeV photons with the appropriate quality cuts mentioned above, to obtain the  $\gamma$ -ray light curves. Since no variability is expected from the underlying background diffuse emission, we fix the normalization of both background components to the best fit values obtained for the whole time period.

Initially, the light curve was calculated with the help of an adaptive binning method. At regular (fixed) time binning, the long bins will smooth out the fast variation while short bins might result in many upper limits during the low-activity periods. In the adaptive binning method, the time bin widths are adjusted to produce bins with constant flux uncertainty above the optimal energies [113] meant to find rapid changes in  $\gamma$ -ray fluxes. The adaptively binned light curve with 15% uncertainty and above  $E_0 = 156.1$  MeV in Fig. 5.1 shows several bright  $\gamma$ -ray states: from MJD 57420 to MJD 57445 and from MJD 57700 to MJD 57900. The peak flux of  $(2.52 \pm 0.42) \times 10^{-5}$  photon  $cm^{-2} s^{-1}$  with a photon index of  $\Gamma = 1.99 \pm 0.15$  was observed on MJD 57738.47 within 4.31 minutes with a convincingly high  $\sim 20.0\sigma$ . It corresponds to a flux of  $(3.55 \pm 0.55) \times 10^{-5}$  photon  $cm^{-2} s^{-1}$  above 100 MeV which  $\sim 221$  times exceeds the average  $\gamma$ -ray flux given in 3FGL ( $\simeq 1.60 \times 10^{-7}$  photon  $cm^{-2} s^{-1}$ ) but the source is variable with a variability index of 1602.3 in 3FGL). In addition, we used gtfindsrc tool to determine the best coordinates of the  $\gamma$ -ray emission in this period, yielding (RA,dec)= (338.115, 11.746) with a 95% confidence error circle radius of  $r_{95} = 0.06$ . These coordinates are offset only by  $0.03^\circ$  from the  $\gamma$ -ray position of CTA 102, indicating that it is the most likely source of the emission. The hardest photon index of  $1.61 \pm 0.10$  ( $22.56\sigma$ ) was observed on MJD 57752.45 within 9.46 minutes, which is significantly harder than the mean photon index observed during the considered period,  $\Gamma_{mean} = 2.22$ .

In the adaptively binned light curve there is a hint at flux changes in minute scales. For example, the interval of MJD 57737.88- MJD 57739.00 ( $\sim 1.13$  days), contains 67 adaptive bins each having a width of the order of a few minutes and a detection significance of  $> 14.3\sigma$ . Another such active period was observed on MJD 57752.0, though the time bin widths were a few tens of minute. Many times during the considered period, the source flux exceeded  $10^{-5}$  photon  $cm^{-2} s^{-1}$ , mostly observed during the extremely active period from MJD 57736.4 to MJD 57798.46 as well as a few times on MJD

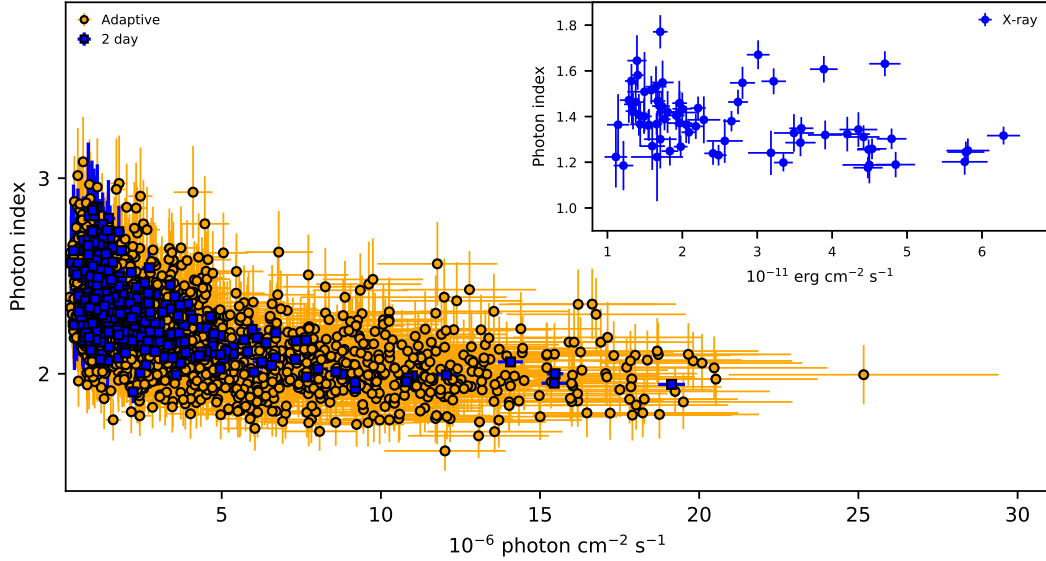


Figure 5.2 CTA 102  $\gamma$ -ray photon index vs. flux in adaptive (orange) and two-day bins (blue). Similar plot for the X-ray band is shown in the insert.

57439.0 and MJD 57862.0. During these periods, the photon flux and index vary within  $(1.01 - 2.52) \times 10^{-5} \text{ photon cm}^{-2} \text{ s}^{-1}$  and  $1.61 - 2.56$ , respectively, the minimum and maximum bin widths being 4.31 and 194.54 minutes and the detection significance varying from  $13.18\sigma$  to  $22.61\sigma$ .

Fig. 5.1 b) shows the  $\gamma$ -ray light curve  $> 1 \text{ GeV}$  (2 days; red color) and  $> 10 \text{ GeV}$  (7 days; blue color) with a noticeable increase in the flux, the peaks being  $(2.32 \pm 0.10) \times 10^{-6} \text{ photon cm}^{-2} \text{ s}^{-1}$  and  $(6.43 \pm 0.94) \times 10^{-8} \text{ photon cm}^{-2} \text{ s}^{-1}$ , at 2-day and 7-day binning, respectively. Above 10 GeV, among 105 total bins only in 36 the detection significance is at least  $4\sigma$ , but, e.g., on MJD 57741.0 and MJD 57748.0 it is as large as  $\simeq 29\sigma$ ,  $N_{pred}$  varying within 46 – 55. The  $\gamma$ -ray photon index variation above 0.1 and 10 GeV is shown in Fig. 5.1 c) with red and blue colors, respectively. There is an obvious hardening above 0.1 GeV, when the photon index changed to  $\Gamma \simeq 2.0$ , during the most bright periods of the source. The mean  $\gamma$ -ray photon index above 10 GeV is  $\Gamma_{mean} = 3.41$  but on MJD 57776.0  $\Gamma = 1.79 \pm 0.55$  with  $7.85\sigma$ .

The  $\gamma$ -ray photon index versus flux is presented in Fig. 5.2 for adaptive (orange) and 2-day binning (blue;  $> 0.1 \text{ GeV}$ ). When 2-day intervals are considered, there is a hint of spectral hardening as the source gets brighter.

In the  $\gamma$ -ray band such behaviour has been already observed from several blazars (e.g., PKS 1502+106 [72], PKS 1510-089 [70], sometimes from 3C 454.3 [77], etc.) and radio galaxies (e.g., NGC 1275 [81]). Such evolution of spectral index and flux is expectable when accelerated HE electrons are cooled down (e.g., [111]). It is hard to see similar relation in the case of adaptive bins as the bright periods last shorter, leading to larger uncertainties. The linear-Pearson correlation test applied to 2-day and adaptively binned intervals yielded  $r_p = -0.569$  and  $r_p = -0.533$ , respectively, the p-value being  $<< 10^{-5}$ . This suggests negative correlation between the flux and photon index, i.e., as the flux increases, the photon index decreases (hardens).

The distribution of highest energy events ( $> 10$  GeV) detected from CTA 102, calculated using the gtsrcprob tool is presented in Fig. 5.1 f). Most of the HE photons are observed during MJD 57700-57800 with the maximum of 97.93 GeV detected on MJD 57773.34.

### 5.2.2 Swift UVOT/XRT observations

The data from seventy Swift (Neil Gehrels Swift observatory) observations of CTA 102 carried out from 01 January 2016 to 09 January 2018 have been analyzed. The exposures range from 0.3 ks (ObsID:33509083) to 3.14 ks (ObsID:33509095) and most of the observations were made in the photon counting and only two in the window timing mode. The XRT data were analyzed with XRTDAS (v.3.3.0) using standard procedure and the most recent calibration databases. Events for the spectral analysis were selected within a 20 pixel (47'') circle with the source at the center, while the background region as an annulus with the same center and having inner and outer radii of 51 (120'') and 85 pixels (200''), respectively. The count rate in some observations was above 0.5 count  $s^{-1}$  implying pile-up in the inner part of the PSF. This effect was removed by excluding the events within a 3 pixel radius circle centered on the source position. The Cash statistics [91] on ungrouped data was used as for some observations the number of counts was low. However for the observations with a high count rate, the results were also cross-checked by rebining to have at least 20 counts per bin and then fitted using the  $\chi^2$  minimization technique. The individual spectra were fitted with XSPEC v12.9.1a adopting an absorbed power-law model with  $N_H = 5.35 \times 10^{20} cm^{-2}$  column density, ignoring the channels with energy below 0.3 keV and above 10 keV. Fig. 5.1 d) shows the X-ray flux evolution in time, where its gradual increase

contemporaneous with the  $\gamma$ -ray flux around MJD 57750 can be seen. The highest flux of  $F_{0.3-10\text{ keV}} \simeq (6.71 \pm 0.21) \times 10^{-11} \text{ erg cm}^{-2} \text{ s}^{-1}$  observed on MJD 57759.69 exceeds the average flux ( $\simeq 1.2 \times 10^{-11} \text{ erg cm}^{-2} \text{ s}^{-1}$ )  $\sim 5.6$  times. A relation between the unabsorbed X-ray flux and photon index is represented in the insert of Fig. 5.2. A trend of a harder spectrum when the source is brighter can be seen. Such harder-when-brighter trend in the X-ray band was already observed from several FSRQs (e.g., PKS 1510-089 [110, 97], 3C 454.3 [144] and etc.) which can be described if assuming the electrons are losing energy mainly through interaction with the external photon fields (e.g., [145]).

The data from the second instrument on board the Swift satellite, UVOT, was used to measure the flux of the source in the UV/optical bands. Photometry was computed using a five-arcsecond source region around CTA 102 and for the background - a source-free annulus centered on the source position with 27'' inner and 35'' outer radii. The magnitudes were computed using UVOT-SOURCE task, then corrected for extinction, using the reddening coefficient E(B-V) from Schlafly & Finkbeiner [136] and the ratios of the extinction to reddening A/E(B-V) for each filter from Fitzpatrick [99] then converting to fluxes, following Breeveld et al. [86]. The flux measured for  $V$ ,  $B$ ,  $U$ ,  $W1$ ,  $M2$  and  $W2$  filters is shown in Fig. 5.1 e). Even if the available data are not enough for detailed studies, it is clear that up to  $\sim$  MJD 57720 the source was in a relatively faint state in the optical/UV band but its flux significantly increased during the bright flaring period around  $\sim$  MJD 57750. This is in agreement with the recent results by Raiteri et al. [130] which show that the source emission in the optical band increased in late 2016 with a 6-7 magnitude jump as compared with the minimal state. The maximum flux in the  $R$ -band was observed on 28 December 2016 (MJD 57750) with a peak luminosity of  $1.32 \times 10^{48} \text{ erg s}^{-1}$ . In addition, the radio monitoring (at 37 GHz) showed that the peak in this band is much earlier than the one in the R-band, inferring these emissions were produced in different locations of the jet.

### 5.2.3 NuSTAR observation

In the hard X-ray band (3-79 keV), CTA 102 was observed once on 30 December 2016 by NuSTAR with a net exposure of  $\sim 26.21$  ks, when it was bright in the X-ray and  $\gamma$ -ray bands. The raw data (from both Focal Plane Modules [FPMA and FPMB; [108]]) were processed with the NuSTAR Data Analysis

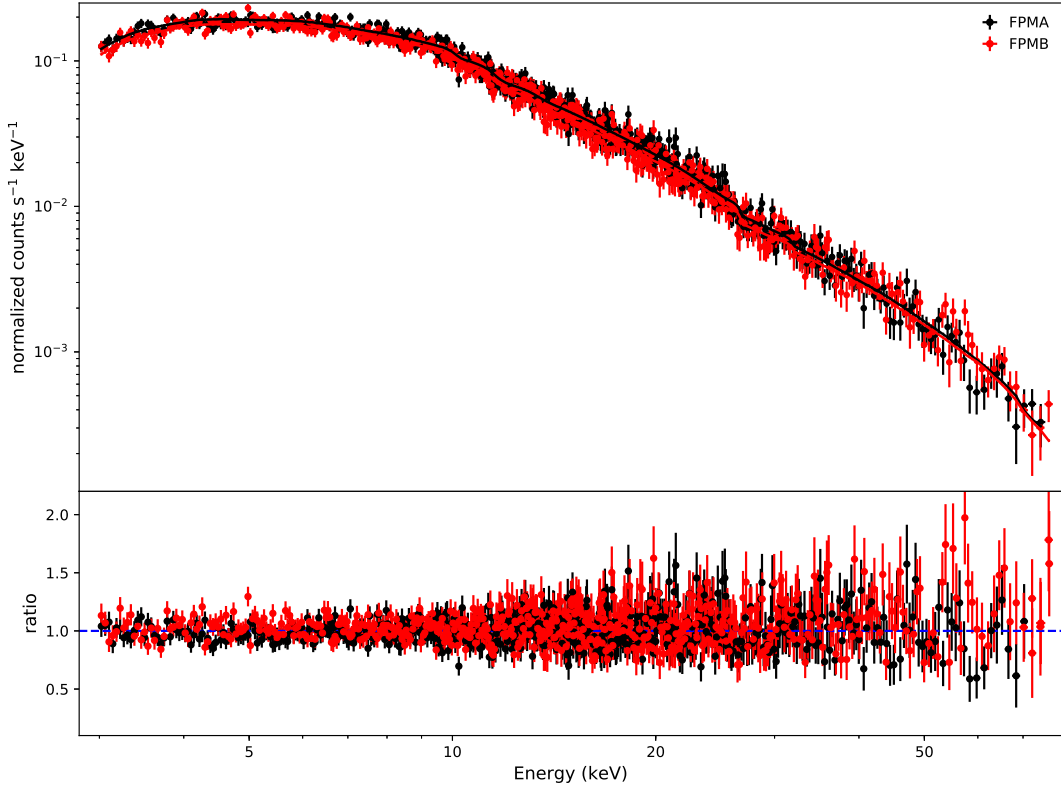


Figure 5.3 Top: NuSTAR FPMA (black) and FPMB (red) spectra and best-fit models. Bottom: Residuals with respect to power-law model.

Software (NuSTARDAS) package v.1.4.1 (via the script nupipeline), producing calibrated and cleaned event files. The events data were extracted from a region of  $75''$  centered on the source position, while the background was extracted from a nearby source free circular region with the same radius. The spectra were binned so to have at least 30 counts per bin and fitted assuming an absorbed power-law model. The best fit resulted in  $\Gamma_X = 1.32 \pm 0.005$  and  $F_{3-79\text{ keV}} \simeq (2.94 \pm 0.02) \times 10^{-10} \text{ erg cm}^{-2} \text{ s}^{-1}$  with  $\chi^2 = 0.97$  for 1131 degrees of freedom. The corresponding spectra for FPMA and FPMB are shown in Fig. 5.3.

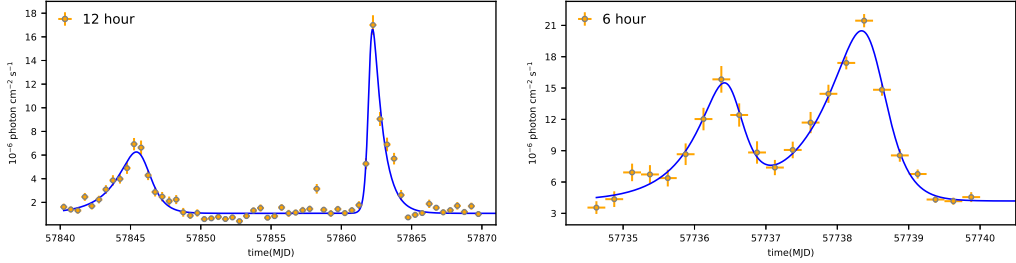


Figure 5.4 Light curves of CTA 102 above 100 MeV with time binning of 6 h (upper panel) and 12 h (lower panel). The lines show the flare fit with Eq. 5.2.1 (Table 5.1).

Table 5.1. Parameter values best explaining the flares.

Flare period $t_0$ MJD	$t_r \pm err$ (day)	$t_d \pm err$ (day)	$F_0/10^{-6}$ photon $\text{cm}^{-2}\text{s}^{-1}$
$57736.53 \pm 0.11^{\text{a}}$	$0.46 \pm 0.13$	$0.17 \pm 0.08$	$18.68 \pm 3.33$
$57738.50 \pm 0.06^{\text{a}}$	$0.60 \pm 0.09$	$0.21 \pm 0.03$	$29.04 \pm 2.39$
$57845.78 \pm 0.36^{\text{b}}$	$1.49 \pm 0.33$	$0.70 \pm 0.23$	$9.72 \pm 1.26$
$57862.02 \pm 0.11^{\text{b}}$	$0.17 \pm 0.06$	$0.73 \pm 0.11$	$25.20 \pm 2.63$

<sup>a</sup> $F_c = (4.18 \pm 0.34) \times 10^{-6} \text{ photon cm}^{-2}\text{s}^{-1}$ .

<sup>b</sup> $F_c = (1.07 \pm 0.08) \times 10^{-6} \text{ photon cm}^{-2}\text{s}^{-1}$ .

### 5.2.4 The light curves variability

The  $\gamma$ -ray (2-day ( $> 0.1$  and  $> 1.0$  GeV), 7-day ( $> 10.0$  GeV) and adaptive binned ( $> 156.1$  MeV)), X-ray (0.3-10 keV) and UV/optical fluxes variation in time are shown in the a), b), c), d) and e) panels of Fig. 5.1. There is an evident major  $\gamma$ -ray flux increase accompanied by moderate brightening in the X-ray and UV/optical bands. The variability in different bands is quantified using their fractional rms variability ( $F_{var}$ ) amplitude [143], resulting in  $F_{var} = 0.511 \pm 0.008$  for X-ray band and correspondingly  $0.920 \pm 0.006$  and  $0.984 \pm 0.004$  for the  $\gamma$ -ray light curves with adaptive and 2-day ( $> 0.1$  GeV) binning, implying much stronger variability in the  $\gamma$ -ray band. This variability is even stronger when the light curves with 2-day ( $> 1.0$  GeV) and 7-day (10.0 GeV) bins are used (excluding correspondingly 20 and 69 periods with upper limits in them), since  $F_{var} = 1.61 \pm 0.01$  and  $1.18 \pm 0.06$ , respectively.

The rapid variability in the  $\gamma$ -ray band can be further investigated by fitting the data with the double exponential form function to obtain the time profiles of the flux variations. However we note that the double exponential form function is not unique and the flare time profiles can be reproduced also by other functions (e.g., see Abdo et al. [71]). As the main purpose of the current fit is only to estimate the rise and decay times, we fit the light curves with the following function [68]:

$$F(t) = F_c + F_0 \times \left( e^{\frac{t-t_0}{t_r}} + e^{\frac{t_0-t}{t_d}} \right)^{-1} \quad (5.2.1)$$

where  $t_0$  is the time of the flare peak ( $F_0$ ) and  $t_r$  and  $t_d$  are the rise and decay times, respectively. Each light curve was fitted with the non-linear optimization python package lmfit<sup>1</sup> using a function that contains two inverses of the sum of exponentials (corresponding to the number of flares).

The active (bright) periods identified in the adaptively binned light curve are analyzed with normal time sampling and only the periods when the rise and decay times can be well constrained are considered. Accordingly, the periods from MJD 57734 to MJD 57740 and from MJD 57840 to MJD 57870 (Fig. 5.4) divided into 6- and 12 hour bins respectively are selected; the detection significance in each bin is  $> 5\sigma$  and the plot of  $N_{pred}/\sqrt{N_{pred}}$  vs  $Flux/\Delta Flux$  shows linear correlation, so the likelihood fit converged for each time bins. The identified four peaks are sequentially numbered from 1 to 4 (F1- F4).

---

<sup>1</sup><https://lmfit.github.io/lmfit-py/>

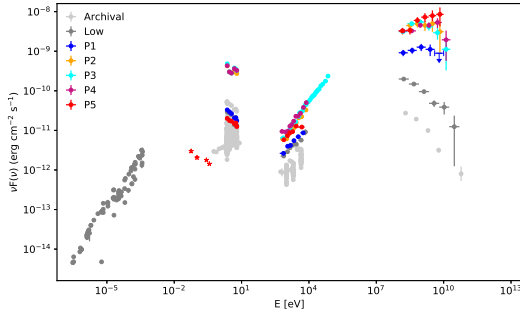


Figure 5.5 The broadband SEDs of CTA 102 in the selected periods. The archival data are shown in light gray.

The fit is shown in Fig. 5.4 and the corresponding parameters are given in Table 5.1. The average flux level ( $F_c$ ) is left free during the fitting and the corresponding values are presented in Table 5.1. The flares 1-3 have rise times longer than the fall, and only F4 shows the opposite tendency. The symmetry of the flares can be quantitatively estimated by calculating the parameter of  $\xi = (t_d - t_r) / (t_d + t_r)$  as defined in Abdo et al. [68] which ranges from  $-0.64$  to  $-0.46$  for F1-3 and  $0.62$  for F4, implying these are moderately asymmetric flares. The shortest e-folding times for rise and decay are  $t_r = 0.17 \pm 0.06$  and  $t_d = 0.21 \pm 0.03$  day<sup>2</sup> observed during F2 and F4, respectively. During F4, when the highest flux was observed within  $4.08 \pm 1.44$  hours, the flux increased up to  $(2.52 \pm 0.26) \times 10^{-5}$  photon cm<sup>-2</sup>s<sup>-1</sup> and dropped to its average level within  $17.52 \pm 2.64$  hour.

### 5.3 Spectral evolution

A "Light curve/SED movie" is made for a better understanding of the spectral evolution in different bands. For each adaptively binned interval, using the estimated photon index and flux, the  $\gamma$ -ray spectra are calculated by dividing the (0.16-300) GeV interval into five logarithmically equal bins. These  $\gamma$ -ray spectra are combined with the UV/optical/X-ray (if available) data to make SEDs. As moving from bin to bin, the spectra in all bands can be compared and their evolution in time seen.

<sup>2</sup>in Table 5.1 e-folding times are given, the doubling or halving timescales can be computed by  $t_{r,d} \times \ln 2$

Table 5.2 Parameters of spectral analysis

<i>Fermi</i>			
Period	Photon Index <sup>a</sup>	Flux <sup>b</sup>	$\sigma^c$
low	$2.39 \pm 0.03$	$1.13 \pm 0.04$	61.4
P1	$2.01 \pm 0.09$	$6.34 \pm 0.72$	25.0
P2	$1.93 \pm 0.08$	$24.17 \pm 2.43$	33.4
P3	$1.96 \pm 0.04$	$24.74 \pm 1.31$	56.5
P4	$1.93 \pm 0.05$	$21.72 \pm 1.40$	48.7
P5	$1.81 \pm 0.08$	$25.14 \pm 2.65$	31.0
Swift-XRT			
Period	Photon Index <sup>d</sup>	Unabsorbed Flux <sup>e</sup>	$\chi^2_{red}$ (d.o.f.)
low	$1.44 \pm 0.05$	$1.45 \pm 0.07$	1.10(39)
P1	$1.41 \pm 0.05$	$1.91 \pm 0.09$	0.77(52)
P2	$1.23 \pm 0.05$	$4.79 \pm 0.22$	0.97(53)
P3	$1.25 \pm 0.04$	$5.75 \pm 0.13$	1.26(84)
P4	$1.32 \pm 0.04$	$6.46 \pm 0.15$	1.20(75)
P5	$1.56 \pm 0.06$	$3.31 \pm 0.15$	0.91(31)
NuSTAR			
P4 <sup>f</sup>	$1.32 \pm 0.005$	$29.36 \pm 0.20$	0.97(1131)

Notes:

N

<sup>a</sup> $\gamma$ -ray photon index from likelihood analysis.

<sup>b</sup> $\gamma$ -ray flux in the  $0.1 - 300$  GeV energy range in units of  $10^{-7}$  photon  $cm^{-2} s^{-1}$ .

<sup>c</sup>Detection significance

<sup>d</sup>X-ray photon index.

<sup>e</sup>0.3–10 keV X-ray flux corrected for the Galactic absorption in units of  $\times 10^{-11}$  erg  $cm^{-2} s^{-1}$ .

<sup>f</sup>X-ray flux and photon index are measured in the energy range 3–79 keV

The movie is uploaded here [youtu.be/K9WWWSy6W8U](https://youtu.be/K9WWWSy6W8U), where the time period from MJD 57620 to MJD 57950 coinciding with the most active  $\gamma$ -ray emitting state is presented. Up to  $\simeq$  MJD 57730, the emission from the source had a soft photon index  $\Gamma \geq 2.0$  and a maximum flux around  $\simeq 10^{-10}$  erg  $cm^{-2} s^{-1}$ , which afterwards exceeded  $10^{-9}$  erg  $cm^{-2} s^{-1}$  with hard  $\gamma$ -ray photon indices. Starting from MJD 57765, the flux dropped to its original level and the  $\gamma$ -ray photon index softened. Around MJD 57800, when the flux increased again, the photon indices were  $\Gamma \simeq 2.0$ , implying a flat spectrum of the source in  $(\nu - \nu F_\nu)$  representation. These spectral evolutions once more confirm a harder-when-brighter trend.

### 5.3.1 Spectral analysis

The data from the following periods are considered for the spectral analyses:

low state (when the source was not flaring in the  $\gamma$ -ray band): when X-ray and  $\gamma$ -ray fluxes were in their average levels: from Swift observations, Obsid: 33509078, 33509079, 33509085, 33509086 and 33509091 were analyzed by merging them to increase the exposure and statistics as they have similar X-ray flux and photon indices while a few intervals, when the source flux exceeded  $9 \times 10^{-7} \text{ photon cm}^{-2} \text{ s}^{-1}$ , were excluded from the contemporaneously obtained  $\gamma$ -ray data. This period corresponds to the pre-flaring state, allowing to investigate the source emission spectrum before the major flare.

Period 1 (P1): MJD 57625.06-57625.39 when the source was in the bright  $\gamma$ -ray state coinciding with XRT observations (Obsid: 33509022 and 33509023, merged during the analyses).

Period (P2): MJD 57738.02-57738.08, bright  $\gamma$ -ray period coinciding with the Swift Obsid: 33509106.

Period 3 (P3):  $\simeq 3.11$  hour period centered on MJD 57752.52, corresponding to a bright  $\gamma$ -ray state coinciding with Swift (Obsid: 33509112 and 88026001, merged) and NuSTAR observations.

Period 4 (P4):  $\simeq 8.06$  hour period centered on MJD 57759.62, corresponding to the period when the highest X-ray flux was observed (Obsid: 33509115).

Period 5 (P5):  $\simeq 14.66$  min period centered on MJD 57862.15, corresponding to another peak of  $\gamma$ -ray emission and available quasi-simultaneous Swift observation on the next day (Obsid: 33509121).

During the unbinned likelihood analyses of *Fermi* data, the spectrum of CTA 102 has been modeled using a power-law function with the normalization and index as free parameters. Then, the SEDs are calculated by fixing the power-law index of CTA 102 and running gtlike separately for smaller energy bins of equal width in log scale. For the spectral analyses the Swift data were binned to have at least 20 counts per bin and then fitted using  $\chi^2$  minimization technique. Then, in order to increase the significance of individual

points in the SEDs calculations, a denser rebinning was applied, restricting the energy range to  $> 0.5$  keV. The results of analyses (both X-ray and  $\gamma$ -ray) are given in Table 5.2 and the corresponding spectra shown in Fig. 5.5.

The  $\gamma$ -ray emission spectra in the low state extended up to  $\sim 10$  GeV with a soft photon index of  $\Gamma = 2.39 \pm 0.03$  while it hardened during the flares, e.g.,  $\Gamma = 1.81 \pm 0.08$  during P5. There is an indication of deviation of the model with respect to the data above several GeV during P3 (cyan data in Fig. 5.5). An alternative fit with functions in the form of  $dN/dE \sim E_\gamma^{-\alpha} \times \text{Exp}(-E_\gamma/E_{cut})$  and  $dN/dE \sim (E_\gamma/E_{br})^{-(\alpha+\beta\log(E_\gamma/E_{br}))}$  were applied to check whether the curvature in the spectrum is statistically significant. The first fit resulted in  $\alpha = 1.64 \pm 0.09$  and  $E_{cut} = 3.84 \pm 1.21$  GeV which is preferred over the simple power-law modeling (comparing log likelihood ratio tests) with a significance of  $4.81\sigma$ . The second fit with  $\alpha = 1.58 \pm 0.10$  and  $\beta = 0.21 \pm 0.05$  is preferred with a significance of  $5.2\sigma$ . The breaks in the emission spectra can be expected from pair production in BLR [129] or can be related with the breaks in the emitting electron spectra [73]. The possible origin of the curvature in the GeV spectra should be investigated deeper, with more detailed spectral analyses of single as well as several flaring periods, which is beyond the scope of the current paper.

## 5.4 Broadband SEDs

Fig. 5.5 shows the broadband SEDs of CTA 102 in its low and active periods together with the archival radio-X-ray data (light gray) from ASI science data center. The WISE IR data are highlighted by red asterisk which are most probably due to the torus emission as the recent studies show that the detection rate of almost all  $\gamma$ -ray blazars was high in the WISE all-sky survey [117]. The comparison shows that during the considered periods the fluxes in the optical/X-ray and  $\gamma$ -ray bands exceed the averaged archival data: the increase is more significant in the optical/UV band. This increase in all bands is expected as the selected periods correspond to the pre-flaring, flaring and post flaring states, and the source shows different emission properties as compared with the averaged spectrum.

Comparing our selected period i) the low-energy component increased while its peak frequency remained relatively constant ( $\leq 10^{15}$  Hz), ii) the second component increased and shifted to HEs with a strong Compton peak dominance and iii) the UV/optical, X-ray and  $\gamma$ -ray fluxes contemporaneously

increased in P2, P3 and P4, while the emission in the UV/optical and X-ray bands was relatively constant in P1 and P5.

The blazar flares can be explained by the changes in the magnetic field, in the emitting region size and its distance from the black hole, bulk Lorentz factor, particle energy distribution, etc. [124]. For example, both emission components will be shifted to HEs when the particles are effectively re-accelerated. Only the HE component will increase when the contribution of the external photon fields starts to dominate, for example, due to the changes in the location of the emitting region [124]. However, these are not unique models for explaining the flaring events. Another possibility is the geometrical interpretation of the origin of flares, the case when the jet regions may have different viewing angles. Such a model with a twisted inhomogeneous jet was already applied to explain the emission from CTA 102 jet in the optical, infrared and radio bands [130]. The photons of different energy come from the jet regions which have different orientations (hence, different Doppler boosting factors) because of the curvature of the jet.

The SEDs obtained in the low state, P1 and P5 showing different features, and in the bright P2 have been modeled. In order to account for Compton dominance, we assume the bulk Lorentz factor ( $\delta$  which equals to the bulk Lorentz factor for small viewing angles,  $\delta \simeq \Gamma$ ) of the emitting region increased from 10 in the low to 20 in the active states (these are typical values estimated for FSRQs [105]). When the SEDs in the low state and in P2 are modeled, the emission from a compact region inside and outside the BLR is discussed. Instead, when modeling the periods with lacking correlation in the  $\gamma$ -ray and UV/optical/X-ray bands, we assume the emission from the radio to X-rays is produced in the extended and slow-moving region unrelated to the flaring component, while the HE  $\gamma$ -rays come from a compact and fast-moving region outside BLR [141].

#### 5.4.1 Modeling the SEDs

The SEDs are fitted within a leptonic scenario that includes synchrotron/Synchrotron Self-Compton (SSC) [103, 85, 115] and External Inverse-Compton (EIC) [139] models. A spherical emission region ("blob") with a radius of  $R$  and  $B$  magnetic field carries relativistic electrons with a  $N'_e(E'_e) = N'_0 (E'_e/m_e c^2)^{-\alpha} \text{Exp}[-E'_e/E'_{cut}]$  distribution for  $E'_e \geq E'_{min}$  where  $E'_{min}$  is the minimum electron energy. The size of the emitting region can be inferred from the observed e-folding timescale

of 4.08 hours from the  $R \leq \delta c t / (1 + z) \approx \delta \times 2.16 \times 10^{14}$  cm relation. For the extended emission component, a region with a ten times larger radius ( $\simeq 4 \times 10^{16}$  cm) will be used.

The low-energy component is modeled by synchrotron emission while for the Inverse Compton (IC) scattering the photons from synchrotron emission, from BLR and dusty torus will be taken into account. The density of BLR ( $u_{BLR}$ ) and dusty torus ( $u_{dust}$ ) are calculated as functions of the distance  $r$  from the black hole by the formulae, (e.g., Sikora et al. [140])

$$u_{BLR}(r) = \frac{L_{BLR}}{4\pi r_{BLR}^2 c [1 + (r/r_{BLR})^3]}, \quad (5.4.1)$$

$$u_{dust}(r) = \frac{L_{dust}}{4\pi r_{dust}^2 c [1 + (r/r_{dust})^4]}. \quad (5.4.2)$$

The estimated size and luminosity of BLR correspondingly are  $r_{BLR} = 6.73 \times 10^{17}$  cm and  $L_{BLR} = 4.14 \times 10^{45}$  erg s $^{-1}$  [125]. The disk luminosity is  $L_{disk} = 10 \times L_{BLR} \simeq 4.14 \times 10^{46}$  erg s $^{-1}$  (assuming its 10% is reprocessed into BLR radiation) then the size and luminosity of torus will be  $R_{dust} = 10^{18} (L_{disc}/10^{45})^{0.5} = 6.43 \times 10^{18}$  cm [123] and  $L_{dust} = \eta L_{disc} = 1.24 \times 10^{46}$  erg s $^{-1}$  ( $\eta = 0.6$ , [102]) a little larger than the value from tentative detection of dust emission in CTA 102 [114]. Moreover, reproducing the near-IR data presented in Fig. 5.5 with a blackbody component requires a luminosity of a few times  $10^{46}$  erg s $^{-1}$  in agreement with the value used. We adopt an effective temperature  $T_{BLR} = 10^4$  K for the BLR radiation and  $T = 10^3$  K for dusty torus.

The model free parameters and their uncertainties are estimated using a Markov Chain Monte Carlo (MCMC) method. We have modified the naima package [146] and the spectral model parameters have been derived through MCMC sampling of their likelihood distributions. For the model free parameters the following expected ranges are considered:  $1.5 \leq \alpha \leq 10$ ,  $0.511$  MeV  $\leq E'_{cut,min} \leq 10$  TeV, and  $N_0$  and  $B$  are defined as positive parameters.

## 5.5 Results and Discussion

The broadband emission from CTA 102 during its bright period in 2016-2018 was investigated. In the  $\gamma$ -ray band, during several periods the flux exceeded  $10^{-5}$  photon cm $^{-2}$  s $^{-1}$  with the maximum being  $(3.55 \pm 0.55) \times 10^{-5}$  photon cm $^{-2}$  s $^{-1}$  (above 100 MeV) observed on MJD 57738.47 which corresponds to an appar-

ent isotropic  $\gamma$ -ray luminosity of  $L_\gamma = 3.25 \times 10^{50} \text{ erg s}^{-1}$  (for a distance of  $d_L = 6.91 \text{ Gpc}$ ). This is one of the highest  $\gamma$ -ray luminosities observed from blazars so far (e.g., see Nalewajko [122]). In the proper frame of the jet, the power emitted in the  $\gamma$ -ray band is  $\sim L_\gamma / 2\delta^2 = 4.06 \times 10^{47} \text{ erg s}^{-1}$  for  $\delta = 20$  which is higher than  $L_{disk}$  in agreement with the results by Ghisellini et al. [106]. During this bright period, on a 6-h timescale, the apparent luminosity was  $\simeq 2.0 \times 10^{50} \text{ erg s}^{-1}$  with the rate of change  $L/\Delta t \simeq 1.89 \times 10^{46} \text{ erg s}^{-2}$  (using  $\Delta t = 6 \text{ h}/(1+z) \simeq 1.06 \times 10^4 \text{ s}$ ), slightly higher than that observed from 3C 454.3 [69] and well above the Elliot-Shapiro relation [98].

The photon index varies as well: the hardest was  $1.61 \pm 0.10$  observed on MJD 57752.45 which is unusual for FSRQs (having an average photon index of 2.4 [75]), while on MJD 57528.63 it was as soft as  $3.08 \pm 0.23$ . The hardest and softest photon indices were observed during the active and low states, confirming the harder-when-brighter trend. The HE photons ( $> 10 \text{ GeV}$ ) were mostly emitted during the active period of MJD 57700-57800, the highest energy photon being 97.93 GeV. The fractional variability parameter  $F_{var}$  shows that the variability is stronger in the  $\gamma$ -ray band ( $F_{var} > 0.9$ ), increasing at higher energies.

The observed flares are asymmetric which might be due to different relations between particle acceleration and emission timescales. For example, the flares decrease much faster (F1-F3) when the accelerated particles start to escape from the emitting region or the cooling time gradually increases. Whereas, the flare will appear with a fast rise and a slow decay trend (F4) when the fast injected energetic particles loose energy or escape from the regions for a longer time. The observed shortest e-folding time is  $\simeq 4.1$  hours, inferring that the emitting region is compact. However, during the brightest periods of  $\sim$ MJD 57738.0 and  $\sim$ MJD 57752.0, several minutes of observations were already enough to have  $> 14.3\sigma$  detection significance, implying shorter time scale variability cannot be excluded (see Shukla et al. [138] for detailed analysis in shorter periods).

Contemporaneous increase in the UV/optical and X-ray bands were also observed during some bright  $\gamma$ -ray periods. In the X-ray band (0.3-10 keV), the maximum flux is  $(6.71 \pm 0.21) \times 10^{-11} \text{ erg cm}^{-2}\text{s}^{-1}$  and the photon index hardens in the bright periods. Comparing the Swift UVOT data obtained in different periods (see Fig. 5.5 and SED/light curve movie) one can see a clear indication of flux increase in the UV/optical bands as well.

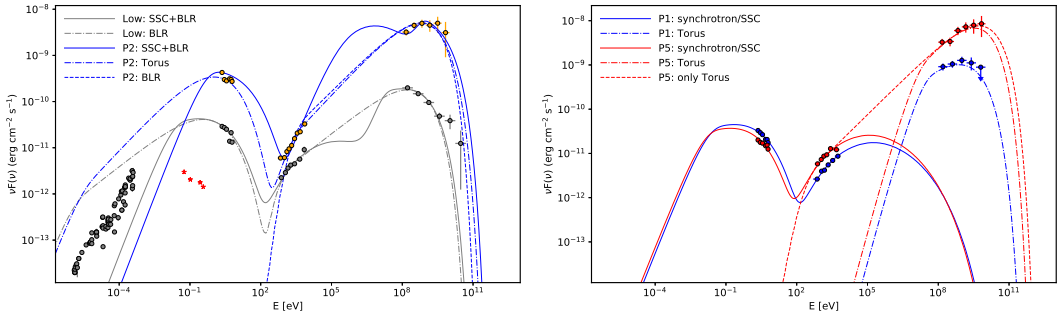


Figure 5.6 Modeling of the broadband SEDs of CTA 102 during the low state and P2 (left panel, gray and orange, respectively) and P1 and P5 (right panel, blue and red, respectively). The model parameters are given in Table 5.3. For the models applied see the text.

### 5.5.1 The origin of the emission

Initially, we modeled the SED observed in the low state (Fig. 5.6; left panel). The radio data are treated as upper limits during the modeling, as the emission in this band is produced from the low-energy electrons which are perhaps from much extended regions. We note that the IR flux predicted by the models exceeds the archival IR data  $\sim 200$  times in the flaring (P2) and 28.7 times in the selected low states (see Fig. 5.6; left panel), implying that the non-thermal synchrotron emission from the jet dominates over the other emission components. When the IC scatterings of both synchrotron and BLR photons are considered, the X-ray data allow to measure  $E'_{min} = 68.25 \pm 5.27$  MeV and  $\alpha = 2.51 \pm 0.11$ . In order to explain the observed UV/optical data, a  $E'_c = 0.67 \pm 0.1$  GeV cut-off is required which makes the SSC component to decay in sub-MeV band and the HE data are described only by IC of BLR photons. Alternatively, both X-ray and  $\gamma$ -ray data can be described by IC scattering of BLR photons (dot-dashed gray line in Fig. 5.6) but the low-energy tail of IC spectra can reproduce the X-ray data only if  $\gamma_{min} = E_e/m_ec^2$  is close to unity [92]. In this case, however, the synchrotron emission of these low energy electrons with  $E_{min} = 0.54 \pm 0.03$  MeV will exceed the observed radio flux, making this scenario unlikely.

Table 5.3. Parameters best describing the multiwavelength emission in different periods.

	low		P1	P2		P5	
	SSC+BLR	BLR	compact	SSC+BLR	Torus	compact	To
$\delta$	10	10	20	20	20	20	
$\alpha$	$2.51 \pm 0.11$	$2.19 \pm 0.02$	$2.12 \pm 0.54$	$2.79 \pm 0.44$	$1.91 \pm 0.03$	$1.78 \pm 0.52$	1.95
$E_{min}[\text{MeV}]$	$68.25 \pm 5.27$	$0.54 \pm 0.03$	$155.59 \pm 109.18$	$227.25 \pm 26.43$	$1.38 \pm 0.15$	$121.33 \pm 67.33$	0.63
$E_c[\text{GeV}]$	$0.67 \pm 0.1$	$0.49 \pm 0.04$	$1.42 \pm 0.81$	$1.32 \pm 0.43$	$0.98 \pm 0.05$	$2.36 \pm 1.54$	3.85
$E_{max} [\text{TeV}]$	$0.57 \pm 0.31$	$0.49 \pm 0.31$	$0.48 \pm 0.34$	$0.50 \pm 0.30$	$0.41 \pm 0.18$	$0.58 \pm 0.25$	0.54
$B[\text{G}]$	$5.40 \pm 0.13$	$5.37 \pm 0.14$	$0.23 \pm 0.29$	$6.10 \pm 0.50$	$1.01 \pm 0.003$	$0.004 \pm 0.042$	0.015
$L_B[\text{erg s}^{-1}]$	$1.75 \times 10^{46}$	$1.73 \times 10^{46}$	$1.47 \times 10^{42}$	$1.04 \times 10^{45}$	$2.86 \times 10^{43}$	$3.86 \times 10^{38}$	6.44
$L_e[\text{erg s}^{-1}]$	$4.66 \times 10^{44}$	$2.90 \times 10^{45}$	$1.73 \times 10^{46}$	$2.84 \times 10^{45}$	$2.74 \times 10^{47}$	$7.33 \times 10^{46}$	1.97

**P2** Fig. 5.6 (left panel) shows the modeling of the SED observed in P2, considering the synchrotron and BLR photons (SSC+BLR, solid line) and then only BLR (dashed line) and only torus (dot-dashed line) photons. When the emitting region is within BLR (SSC+BLR), the hard X-ray spectra  $1.23 \pm 0.05$  can be explained only when  $E'_{min} = 227.25 \pm 26.43$  MeV and  $\alpha = 2.79 \pm 0.44$ , while  $E'_c = 1.32 \pm 0.43$  GeV and  $B = 6.10 \pm 0.50$  G are estimated from the low-energy component. Also, the external photon fields can dominate for the IC scattering as their density will increase  $\Gamma^2$  times in the jet frame. For example, the required parameters (especially  $B$ ) can be somewhat softened when only the IC of torus photons is considered (see Table 5.3). In the case of only BLR photons, the low-energy tail of IC spectra will decline at  $\sim \gamma^2 \epsilon_{BLR} \simeq 0.52$  keV (dashed line in Fig. 5.6 left panel), contradicting Swift XRT data (unless lower  $\delta$  is used). This modeling shows that during the bright  $\gamma$ -ray periods the emission can be also produced outside the BLR. At low energies, the model flux overpredicts noncontemporaneous radio data, but when taking the synchrotron self-absorption into account, which dominates below the frequencies  $\sim 10^{13}$  Hz (calculated following Rybicki & Lightman [132]), the synchrotron flux will be below the radio data. We note that simultaneous observations at low energies, which are missing in this case, are crucial for better constraining of the model free parameters and for deriving some limits/constraints on the source emission properties. As the models presented in Fig. 5.6 (left panel) predict different spectra and fluxes at GHz or mid-IR

range, the observations at these bands can be also used to distinguish between these two models.

**P1 and P5** Fig. 5.6 (right panel) shows the results of a two-zone SEDs modeling. For the emission from the extended blob we fixed all the parameters, except  $B$  and  $N_0$ , to the values obtained from the fitting of the SED in the low state, as in the UV/optical and X-ray bands the flux and photon indices did not change significantly (Fig. 5.5). In addition, all the parameters of the compact blob are free, but it is required that its synchrotron emission has no contribution at lower energies.

As compared with the low state, the magnetic field in the extended blobs is estimated to be low,  $5.05 \pm 0.08$  G and  $3.43 \pm 0.05$  G for P1 and P5, respectively, implying the modest X-ray flux changes are related with the increase of electron density. The  $\gamma$ -ray emission is produced in the interaction of fresh electrons (hard power law index  $\leq 2.1$ ) with the torus photons in the compact, fast-moving and particle-dominated blob  $U_e/U_B \geq 10^4$  (Fig. 5.6 right panel). The cut-off energies (defined by the last point in the *Fermi* data) should be considered as lower limits, since there is no indication of break in the  $\gamma$ -ray spectra. In Fig. 5.6 (right panel) the red dot-dashed line shows an alternative modeling, when both X-ray and  $\gamma$ -ray data are modeled by the IC scattering of torus photons. Within such a scenario, the flare is mainly due to the injection/cooling of  $> 10$  GeV electrons, which are affecting only the HE spectra having small contribution to the X-ray band (e.g., the density at lower energies increases due to the cooling of HE electrons). Again, the low energy component should be necessarily produced in a different blob, otherwise its relatively constant peak frequency cannot be explained.

**Jet energetics** The total power of the jet,  $L_{jet} = L_B + L_e$  where  $L_B = \pi c R_b^2 \Gamma^2 U_B$  and  $L_e = \pi c R_b^2 \Gamma^2 U_e$  (e.g., [93]), is of the order of  $L_{jet} \simeq 2 \times 10^{46} \text{ erg s}^{-1}$  in the low state and can be as large as  $\simeq 3 \times 10^{47} \text{ erg s}^{-1}$  during the flares.

When the low and high energy components are contemporaneously increased the required maximum energy of electrons ( $E_c$ ) reaches only a few GeV constrained by the low energy data (the energy of synchrotron photons is proportional to  $\sim \delta B E_e^2$ ). Therefore, during these intense  $\gamma$ -ray flares, the acceleration mechanisms are not effective enough or the electrons cool faster and do not reach HEs. On the other hand, when the  $\gamma$ -ray and UV/optical/X-ray fluxes are uncorrelated, the  $\gamma$ -rays are perhaps produced in a different

part of the jet that contains fresh electrons which can emit up to HE and VHE bands.

## 5.6 Conclusions

We report the results on the observations of CTA 102 in the UV/optical, X-ray and  $\gamma$ -ray bands from January 2016 to January 2018 when the source was in the bright and active states. Generally, the flares are roughly correlated in all these bands but the variability is more prominent in the  $\gamma$ -ray band with several bright flares when the  $\gamma$ -ray flux is substantially increased and the photon index is hardened, showing a harder-when-brighter trend. The measured hardest photon index  $\Gamma = 1.61 \pm 0.10$  significantly differs from the average  $\gamma$ -ray photon index of CTA 102 and is unusual for FSRQs. The highest  $\gamma$ -ray flux measured by *Fermi* is  $(3.55 \pm 0.55) \times 10^{-5} \text{ photon cm}^{-2} \text{ s}^{-1}$  (above 100 MeV) observed on MJD 57738.47, corresponding to an extremely high isotropic  $\gamma$ -ray luminosity of  $L_\gamma = 3.25 \times 10^{50} \text{ erg s}^{-1}$ .

We discussed the origin of the multiwavelength emission from CTA 102 in the framework of the one-zone and multi-zone synchrotron, SSC and EIC scenarios. We assumed a compact ( $R \leq \delta \times 2.16 \times 10^{14} \text{ cm}$  inferred from 4.08 hours  $\gamma$ -ray flux variation) blob inside and outside the BLR. In a single emitting region, the inverse-Compton up-scattering of both synchrotron and BLR photons can explain the data observed in the low state, whereas the contribution of torus photons is essential in the flaring periods. When in the flaring periods the fluxes in the UV/optical, X-ray and  $\gamma$ -ray bands are unrelated, the two-zone models (with an extended blob inside and a compact fast-moving one outside the BLR) can well explain the observed data under reasonable assumptions on the required parameters. These periods appear to be more favorable for the HE emission from CTA 102 as the emitting electrons have higher cut-off energies and harder power-law indices. Most likely, the emission in these periods is produced in the regions outside BLR that contain fresh electrons which dominantly cool due to the inverse-Compton scattering making the variability more evident in the  $\gamma$ -ray band.

# 6 Dissecting the region around IceCube-170922A: the blazar TXS 0506+056 as the first cosmic neutrino source

## 6.1 Introduction

The IceCube Neutrino Observatory at the South Pole<sup>1</sup> has recently reported the detection of a number of high-energy astrophysical neutrinos<sup>2</sup> [147, 177, 178, 179]. These include 82 high-energy starting events collected over six years [182], which are inconsistent with a purely atmospheric origin with a significance greater than  $6.5\sigma$ . The IceCube signal, including the 34 through-going charged current  $\nu_\mu$  from the northern sky [148, 180, 149, 181], is still compatible with an isotropic distribution. The origin of the IceCube neutrinos is presently unknown [see, e.g. 155, and references therein, for a comprehensive discussion] although various hints consistently point to blazars as one of the most probable candidates, as described below.

The Large Area Telescope (LAT) on-board the Fermi Gamma-ray Space Telescope is a pair-conversion telescope sensitive to high energy photons with energies from 20 MeV to greater than 300 GeV [158] that has been surveying the  $\gamma$ -ray sky for the past almost 10 years. The constant monitoring and archiving of all-sky  $\gamma$ -ray data permits unprecedented investigations of variable sources.

To explore the complexity of the multi-wavelength sky, we make use of innovative tools that are under development within “Open Universe”, a new initiative under the auspices of the United Nations Committee On the Peaceful Uses of Outer Space (COPUOS). The goal of Open Universe is to stimulate

---

<sup>1</sup><http://icecube.wisc.edu>

<sup>2</sup>In this paper neutrino means both neutrino and anti-neutrino.

## 6 Dissecting the region around IceCube-170922A: the blazar TXS 0506+056 as the first cosmic neutrino source

---

a large increase of the accessibility and usability of space science data in all sectors of society from the professional scientific community, to universities, schools, museums, and citizens. A web portal of the Open Universe initiative, developed at the Italian Space Agency, is available at [openuniverse.asi.it](http://openuniverse.asi.it). In this paper we make use of software, such as the VOU-BLAZAR tool, which has been specifically designed to identify blazars based on multi-frequency information in large error regions, and spectral energy distribution (SED) animations.

Blazars are active galactic nuclei [AGN; see 202, for a recent AGN review] having a relativistic jet that is seen at a small angle with respect to the line of sight. The jet contains charged particles moving in a magnetic field emitting non-thermal radiation over the entire electromagnetic spectrum [210, 202]. Since the energy distribution of these particles can significantly differ from object to object, the electromagnetic emission exhibits a wide range of intensity levels and spectral slopes across the spectrum. This results in observational properties that depend strongly on the energy band where blazars are discovered. In a series of papers [168, 171, 200, 172] proposed a new blazar paradigm [but see 167, for an alternative scenario] based on dilution by the jet and the host galaxy, minimal assumptions on the physical properties of the non-thermal jet emission, and unified schemes. By means of detailed Monte Carlo simulations, it was shown that this scenario is consistent with the complex observational properties of blazars as we know them in all parts of the electromagnetic spectrum.

The possibility that blazars could be the sources of high-energy neutrinos has been investigated by many authors, even long before the IceCube detections [e.g. 194, 174, 197, 199, 205, 208].

[201] have correlated the second catalogue of hard Fermi-LAT sources (2FHL,  $E > 50 \text{ GeV}$ , Ackermann et al. 154) and other catalogues, with the publicly available high-energy neutrino sample detected by IceCube. The chance probability of association of 2FHL high-energy peaked blazars (HBL/HSP, i.e. sources with the peak of the synchrotron emission  $\nu_{peak}^S > 10^{15} \text{ Hz}^3$ ; Padovani & Giommi 198) with IceCube events was 0.4 per cent, which becomes 1.4 per cent ( $2.2\sigma$ ) by evaluating the impact of trials [206]. This hint appears to be strongly dependent on  $\gamma$ -ray flux. The corresponding fraction of the IceCube signal explained by HBL is however only  $\sim 10 - 20$  per cent, which

---

<sup>3</sup>Blazars can be further divided into low (LBL:  $\nu_{peak}^S < 10^{14} \text{ Hz}$ ) and intermediate (IBL:  $10^{14} \text{ Hz} < \nu_{peak}^S < 10^{15} \text{ Hz}$ ) energy peaked sources.

agrees with the results of [150, 183], who by searching for cumulative neutrino emission from blazars in the second Fermi-LAT AGN [2LAC; 152] and other catalogues (including also the 2FHL), have constrained the maximum contribution of known blazars to the observed astrophysical neutrino flux to < 27 per cent.

High-energy astrophysical neutrinos originate in cosmic ray interactions providing a natural link with high-energy and possibly ultrahigh-energy cosmic ray (UHECR) detection. [206] have presented a hint of a connection between HBL, IceCube neutrinos, and UHECRs ( $E \geq 52 \times 10^{18}$  eV) with a probability  $\sim 0.18$  per cent ( $2.9\sigma$ ) after compensation for all the considered trials. Even in this case, HBL can account only for  $\approx 10$  per cent of the UHECR signal.

None of the possible neutrino counterparts in [201] and [206] are tracks, as they are all cascade-like events<sup>4</sup>. This indicates that by using tracks we are still limited in sensitivity to the HBL neutrino signal. Although tracks trace only about 1/6 of the astrophysical signal for a flavour ratio  $\nu_e : \nu_\mu : \nu_\tau = 1 : 1 : 1$ , standard neutrino cross-sections, and IceCube event selection efficiencies, after a long enough exposure a track IceCube signal from blazars should also start to appear. This is of great interest, because false (random) associations of tracks with a blazar are unlikely due to the better defined position of this event-class with respect to cascades.

Recently [192] have found a transient  $\gamma$ -ray ( $> 100$  MeV) AGILE source positionally coincident with an IceCube track with a post-trial significance  $\sim 4\sigma$  and possibly associated with an HBL. However, no other space missions nor ground observatories have reported any detection of transient emission consistent with this event.

The most probable hint of an association ( $3 - 3.5\sigma$ ) reported so far [184] between an IceCube astrophysical neutrino and an extragalactic object is that of the neutrino IceCube-170922A and the radio bright ( $\sim 1$  Jy at 5 GHz) and  $\gamma$ -ray flaring BL Lac object TXS 0506+056 (also known as 5BZB J0509+0541, 2FHL J0509.5+0541, and 3FGL J0509.4+0541). Moreover, IceCube has reported in [185] an independently observed  $3.5\sigma$  excess of neutrinos from the direction of TXS 0506+056 between October 2014 and February 2015 providing further indication of a high-energy neutrino association.

---

<sup>4</sup>The topology of IceCube detections can be broadly classified in two types: (1) cascade-like, characterized by a compact spherical energy deposition, which can only be reconstructed with a spatial resolution  $\approx 15^\circ$ ; (2) track-like, defined by a dominant linear topology from the induced muon, with positions known typically within one degree or less.

## 6 Dissecting the region around IceCube-170922A: the blazar TXS 0506+056 as the first cosmic neutrino source

---

The presence of several non-thermal objects including variable blazars within 80 arc-minutes of IceCube-170922A (that is within the size of the Fermi-LAT point spread function [PSF<sup>5</sup>], which is  $\sim 2.8^\circ$  [95 per cent containment] at  $E = 1\text{ GeV}$ ) makes the  $\gamma$ -ray emission from this area quite complex, with possible source confusion. Different objects could in fact contribute to the overall  $\gamma$ -ray flux at different levels in a time-dependent manner. For this reason, we report here on what we have called the dissection of the region around IceCube-170922A taking into account the fact that all sources present in the area could be in principle contributors to the neutrino emission observed in 2014–2015 and in 2017. We use innovative software tools that exploit all the publicly available multi-frequency data to study in detail the area around the position of IceCube-170922A at all energies and in the time domain, together with a very careful analysis of the  $\gamma$ -ray emission, providing a wide perspective in space and time.

Section 2 describes the multi-messenger data we used, while Section 3 puts them all together to study the relevant sources in the area, their  $\gamma$ -ray light curves and SEDs. Section 4 gives our results, which are discussed in Section 5. Section 6 summarizes our conclusions. We use a  $\Lambda$ CDM cosmology with Hubble constant  $H_0 = 70\text{ km s}^{-1}\text{ Mpc}^{-1}$ , matter density  $\Omega_{m,0} = 0.3$ , and dark energy density  $\Omega_{\Lambda,0} = 0.7$ .

## 6.2 Multi-messenger data analysis

### 6.2.1 Neutrino data

#### The IceCube-170922A alert event

The high-energy upward-going muon IceCube-170922A reported by IceCube through a Gamma-ray Coordinates Network Circular on MJD 58018 [September 22, 2017; 190] originates from a neutrino with  $E_\nu \sim 290\text{ TeV}$ , which is probably of astrophysical origin. The best-fit reconstructed position is right ascension (RA)  $77.43^{+0.95}_{-0.65}$  and declination (Dec)  $+5.72^{+0.50}_{-0.30}$  (deg, J2000, 90 per cent containment region: IceCube Collaboration 184). No other high-energy neutrino passing the same selection of alert-like events has been observed from this direction from 2010 onwards until today.

---

<sup>5</sup>The Fermi PSF for this analysis event selection has been determined using the gtpsf Fermi Science Support Center tool.

[184] have derived the coincidence probability as a measure of the likelihood that a neutrino alert like IceCube-170922A is correlated by chance with a flaring blazar, considering the large number of known  $\gamma$ -ray sources and the modest number of neutrino alerts. This has been done through several hypothesis tests covering a range of assumptions on the spatial and temporal signal distribution and neutrino emission scenarios. The derived probability was trial-corrected by multiplying the p-value by 51, which correspond to the number of alerts issued by IceCube (10) plus the 41 inspected archival events, which would have triggered alerts if the realtime system had been operational. The final post-trial coincidence probability ranges between  $2.5 \times 10^{-4}$  and  $1.3 \times 10^{-3}$  ( $3 - 3.5\sigma$ ).

### The IceCube neutrino flare in 2014–2015

In contrast with the neutrino alert discussed above, which is a single event identified in real time and satisfying stringent selection criteria, we define here a neutrino flare as a statistically significant ( $> 3\sigma$ ) accumulation of neutrinos coming from a specific direction over a well-defined time period.

As reported in [185], the investigation of the historical 9.5 years of IceCube data at the position of TXS 0506+056 revealed an excess with a post-trial coincidence probability  $2 \times 10^{-4}$  ( $3.5\sigma$ ) over  $110_{-24}^{+35}$  days corresponding to a  $\nu_\mu$  fluence at 100 TeV of  $2.1_{-0.7}^{+0.9} \times 10^{-4}$  TeV cm $^{-2}$ , spectral index  $\gamma = 2.1 \pm 0.2$ , and an energy range (68 per cent) between 32 TeV and 3.6 PeV ( $3.6 \times 10^{15}$  eV)<sup>6</sup>. This could be interpreted as the first evidence of high-energy neutrino emission from the direction of a known source and comes from an excess of  $\sim 13$  neutrino events between MJD 56949 and 57059 (October 19, 2014 – February 6, 2015).

#### 6.2.2 Radio and optical monitoring data

The radio (15 GHz) and optical ( $V_{mag}$ ) data have been taken from the Owens Valley Radio Observatory (OVRO<sup>7</sup>) database, the Catalina Real time Tran-

---

<sup>6</sup> We use here the results obtained for the Gaussian time window because they are the most significant.

<sup>7</sup><http://www.astro.caltech.edu/ovroblazars/>

## *6 Dissecting the region around IceCube-170922A: the blazar TXS 0506+056 as the first cosmic neutrino source*

---

sient Survey (CRTS<sup>8</sup>) and from the All Sky Automatic Survey (ASAS<sup>9</sup>; Kochanek et al. 189) online services.

### **6.2.3 X-ray and optical/UV data**

The Neil Gehrels Swift observatory [166] carried out a total of 92 observations within 80 arc-minutes of IceCube-170922A. Of these, 35 were performed before the arrival of the neutrino and were mostly pointed at the nearby flat spectrum radio quasar (FSRQ) PKS 0502+049. The remaining pointings have been carried out either as a Target of Opportunity follow up mapping the error region of IceCube-170922A a few hours after the event [186], or as part of the monitoring program of the blazar TXS 0506+056 triggered by the IceCube neutrino alert.

We have analyzed all 92 X-Ray Telescope [XRT; 161] observations using the latest version of the Swift data reduction software (HEADAS 6.22) applying standard procedures. This led to the detection of 251 X-ray sources, which were combined with those of existing X-ray catalogues to build Fig.6.1 (left). X-ray spectral data were used together with the available multi-frequency data to assemble the SEDs of all interesting sources in the field (see Sect. 6.3.1).

All optical and UV data of the Swift Ultra-Violet and Optical telescope [UVOT; 207] for TXS 0506+056 and PKS 0502+049 were analyzed using the SSDC online interactive archive<sup>10</sup>.

The NuSTAR hard X-ray observatory [175] was pointed twice, on September 29 and October 19 2017, at TXS 0506+056 following the detection of IceCube-170922A. A few days after the observations the data were made openly available. We have analyzed these data sets using the online analysis tool of the SSDC archives following the standard procedure. In both observations the spectral shape shows a sharp hardening at about 4 – 5 keV.

### **6.2.4 $\gamma$ -ray data**

We used publicly available Fermi-LAT Pass 8 (with the P8R2\_SOURCE\_V6 instrument response functions) data acquired in the period from August 4, 2008

---

<sup>8</sup><http://crts.caltech.edu>

<sup>9</sup><http://www.astrouw.edu.pl/asas/>

<sup>10</sup><http://www.asdc.asi.it>

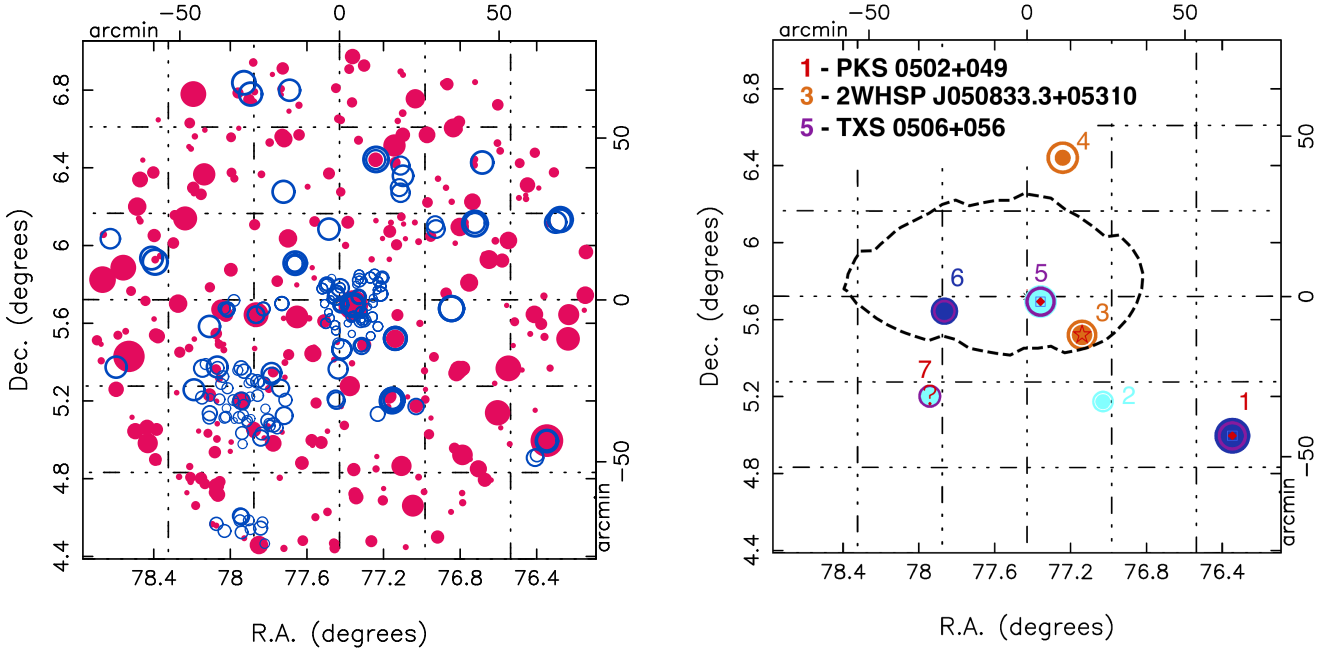


**Figure 6.1 Left:** Radio and X-ray sources within 80 arc-minutes of the position of IceCube-170922A. Symbol diameters are proportional to source intensity. Radio sources appear as red filled circles, X-ray sources as open blue circles. **Right:** Known and candidate blazars around IceCube-170922A as detected by a tool developed within the framework of the Open Universe initiative as described in the text. Dark blue circles represent LBL type candidates, that is sources with flux ratio in the range observed in the sample of LBL blazars of the latest edition of the BZCAT catalogue [195], cyan symbols are for IBL type candidates, and orange symbols are for HBL candidates. Known blazars are also marked by a red diamond if they are included in the BZCAT catalogue or a star if they are part of the 2WHSP sample (see text for sources n. 2, 4, 6, and 7). The diameters of filled and open circles are proportional to radio flux density and X-ray flux, respectively. The dashed line shows the 90 per cent error contour of IceCube-170922A. The localization of the Fermi sources is such that the error ellipses are smaller than the size of the symbols.

## 6 Dissecting the region around IceCube-170922A: the blazar TXS 0506+056 as the first cosmic neutrino source

---

to February 10, 2018 and followed the standard procedures suggested by the Fermi-LAT team. Only the events with a high probability of being photons (`evclass = 128`, `evtype = 3` [FRONT+BACK]) in the energy range of 100 MeV – 300 GeV from a region of interest (ROI) defined as a circle of radius 12° centred at the  $\gamma$ -ray position of TXS 0506+056 (RA, Dec = 77.364, 5.699) were analyzed. We removed a possible contamination from the Earth limb by cutting out all the events with zenith angle  $> 90^\circ$  and only used the time intervals in which the data acquisition of the spacecraft was stable (`DATA_QUAL && LAT_CONFIG==1`). Consistently with the event selection we used the standard Galactic (`gll_iem_v0611`) and isotropic (`iso_P8R2_SOURCE_V6_v0611`) models to describe the diffuse background emissions.

### Test Statistic maps

To evaluate the presence of relevant  $\gamma$ -ray signatures around the arrival direction of IceCube-170922A, we built test statistics (TS) maps of the region [196]. The test statistic for all the  $\gamma$ -ray analysis in this paper is defined as

$$TS = 2 \times [\ln \mathcal{L}(\text{source}) - \ln \mathcal{L}(\text{nosource})], \quad (6.2.1)$$

where  $\mathcal{L}(\text{source})$  represents the nested likelihood of the data given a specific source hypothesis and  $\mathcal{L}(\text{nosource})$  the likelihood of the background model. In our TS maps the signal hypothesis of a  $\gamma$ -ray point source is tested against a background model consisting of a diffuse Galactic and a diffuse isotropic component, as well as all the the Fermi-LAT third source catalogue [3FGL; 151] sources that lie outside the region of the TS map. While the point source is modeled using a power-law with free normalization and spectral index, the parameters of the background sources remain fixed. According to Wilks' theorem the test-statistic distributions follows a  $\chi^2$  distribution with two degrees of freedom. Hence TS values of 30 and 8 are equivalent to a 5 and  $2\sigma$  significance, respectively. We centred our  $80 \times 80$  arc-minute maps at IceCube-170922A and used an equally spaced grid with 0.05° step size in right ascension and declination. For each of the grid points the Fermi Science Tools unbinned likelihood analysis tool `gtlike` was used to maximize the likelihoods in eq. (6.2.1) with respect to the free parameters. We built TS maps for different time windows and energy cuts, resolving the  $\gamma$ -ray activity during the periods of the neutrino detections and for energy thresholds 1 GeV, 2 GeV,

---

<sup>11</sup><https://fermi.gsfc.nasa.gov/ssc/data/access/lat/BackgroundModels.html>

and 5 GeV. Our choices are driven by the the need for sufficiently high space resolution to distinguish different  $\gamma$ -ray sources (as the PSF decreases with energy) and by the fact that, given the possible neutrino production scenarios, we are mostly interested in the photons at the highest energies.

### Light curve and photon index

$\gamma$ -ray flux and photon index variations were investigated using light curves generated with a fixed time binning of 55 ( $28^{12}$ ) days for TXS 0506+056 (PKS 0502+049) and with an adaptive binning method with a constant relative flux uncertainty [191]. In the fixed time binned light curve, photons in the 2 – 100 GeV and 0.1 – 100 GeV ranges were used for TXS 0506+056 and PKS 0502+049, respectively (see below). In the adaptive binning light curve analysis for PKS 0502+049 the fluxes are computed above an optimum energy of  $E_{min} = 214$  MeV in order to reach the required constant relative flux uncertainty of 15 per cent. For all the light curves the flux normalization and photon index of the target source are determined by applying the `gtlike` tool in each time bin. The model file, describing the ROI, contains point sources from the 3FGL catalogue within  $ROI + 5^\circ$  from the target, as well as the Galactic and isotropic  $\gamma$ -ray background models. It is generated using the user contributed `make3FGLxml1.py`<sup>13</sup> tool. For the case of TXS 0506+056 the chosen energy threshold of 2 GeV efficiently removes any source confusion (see Fig. 6.4 and section 6.3.3), hence only this source is left free for the fit. The resulting light curve is robust against mis-modelling and strong time-variability of the other sources in the ROI. The light curve of PKS 0502+049, on the other hand, is derived by reaching lower energies, since the majority of the photons are below 1 GeV [151]. In the source model both sources are fitted at the same time. The diffuse background components are fixed to their nine year value, since they are not expected to vary on the time scales of this analysis. Additionally, since we are using short integration times, we model PKS 0502+049 with a power-law.

---

<sup>12</sup>This difference is due to the fact that the photon statistics for PKS 0502+049 is better than for TXS 0506+056 for the chosen energy thresholds. The bin sizes used have been chosen in order to have enough photon statistics in the majority of the bins but also to avoid any fine tuning.

<sup>13</sup><https://fermi.gsfc.nasa.gov/ssc/data/analysis/user/>

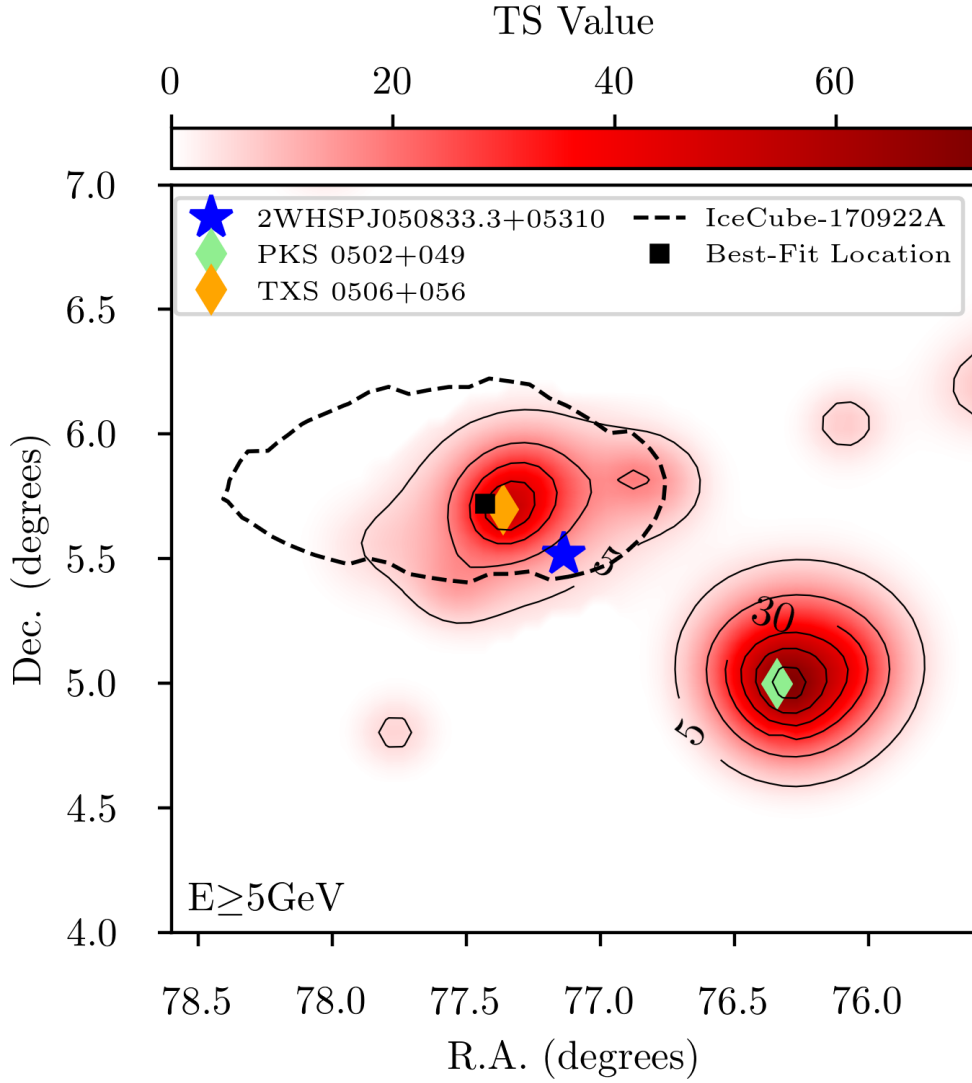


Figure 6.2 Fermi TS map based on photons with energy larger than 5 GeV between MJD 55762 and 55842 (July 20 – October 8, 2011). The dashed line shows the 90 per cent error contour of IceCube-170922A with best-fit location indicated as a black square. The solid contour lines connect points with the same TS value. Linear interpolation has been applied between the bins.

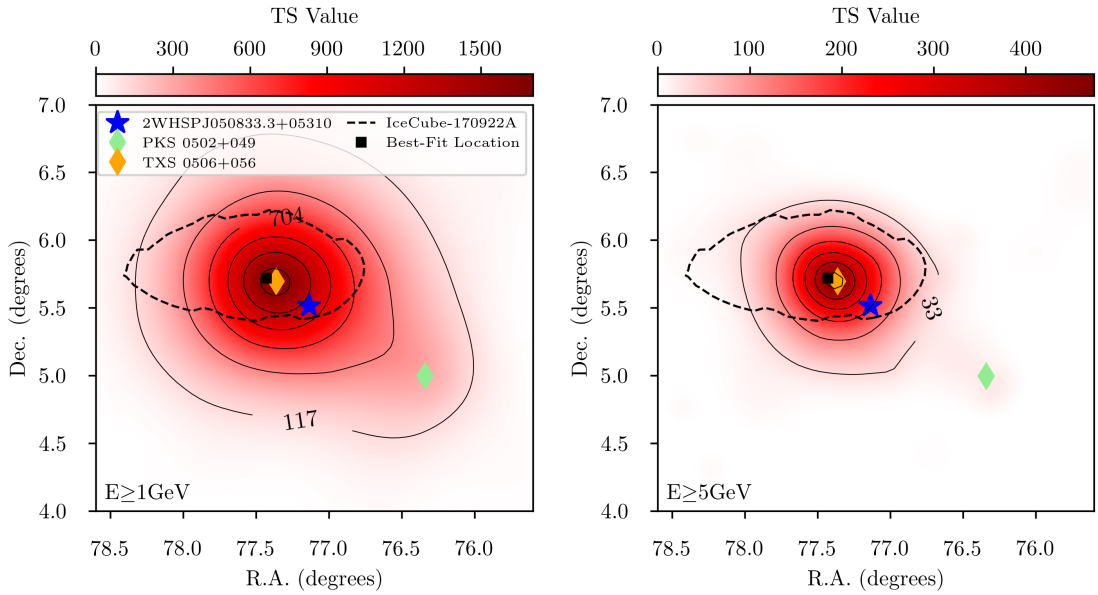


Figure 6.3 Fermi TS map based on photons with energy larger than 1 GeV (left) and 5 GeV (right) between MJD 57908 and 58018 (June 4 – September 22, 2017). In this period TXS 0506+056 is in outburst and dominates the field. See Fig. 6.2 for more information.

## 6 Dissecting the region around IceCube-170922A: the blazar TXS 0506+056 as the first cosmic neutrino source

---

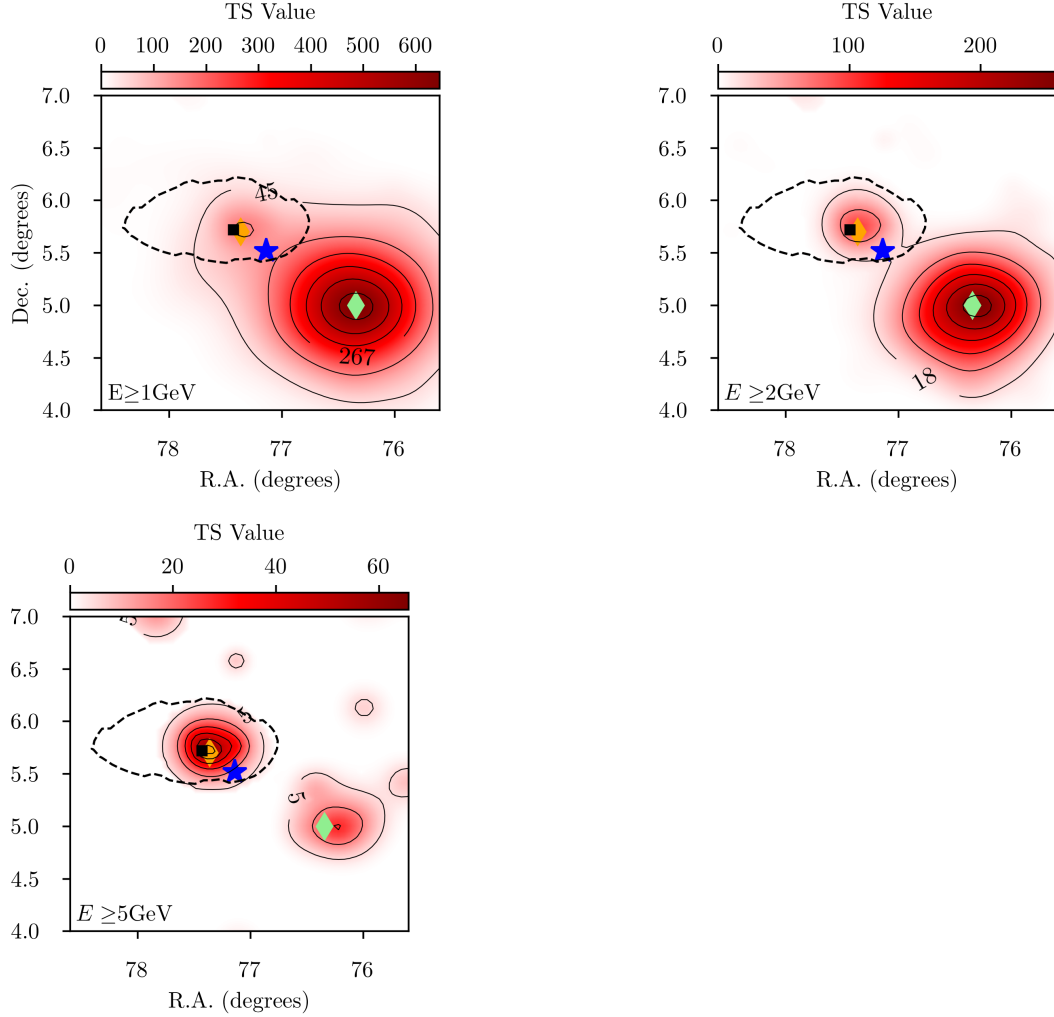


Figure 6.4 Fermi TS map based on photons with energy larger than 1, 2 and 5 GeV between MJD 56949 and 57059 (October 19, 2014 – February 6, 2015). In this period the brightest source was PKS 0502+049 at lower energies while TXS 0506+056 dominated at higher energies. See Fig. 6.2 for more information.

## 6.3 Putting it all together

### 6.3.1 Relevant astronomical sources in the region of IceCube-170922A

We have searched for non-thermal emission in blazar-like sources in the vicinity of IceCube-170922A using a tool that is being developed in the framework of the United Nations Open Universe initiative<sup>14</sup> using Virtual Observatory protocols. This was used to find sources in all available lists of radio and X-ray emitters. Fig. 6.1 (left) shows a plot of the 637 radio and X-ray sources present in those catalogues or which were detected in dedicated Swift observations within 80 arc-minutes of the position of IceCube-170922A. Of these, only 7 emit in both bands and are all blazar-like in their X-ray-to-radio flux ratio, as determined from the BZCAT [195] and 2WHSP [162] samples. These are shown in Fig. 6.1 (right).

Three known objects, i.e. TXS 0506+056 (an IBL/HBL<sup>15</sup> at  $z = 0.3365$ : Pianino et al. 203), PKS 0502+049 (also known as 5BZQ J0505+0459, an LBL/FSRQ at  $z = 0.954$ ), and 2WHSP J050833.3+05310 (an HBL), i.e. sources no. 5, 1, and 3 respectively in Fig. 6.1 (right), and four additional blazar candidates are present in the area. The first two blazars are also bright  $\gamma$ -ray emitters (Sect. 6.3.2). Visual inspection of the SED of the other sources allowed us to confirm that source no. 4 is a good candidate HBL object, while source 7 is likely a cluster of galaxies (due to its extended X-ray emission), source 6 is a steep radio spectrum object, and source 2 is a nearby ( $z = 0.03677$ ) elliptical galaxy showing low luminosity X-ray emission ( $L \sim 10^{41}$  erg s<sup>-1</sup> at 1 keV) that could be due to a jet or even to non-nuclear sources.

### 6.3.2 $\gamma$ -ray emission near IceCube-170922A

The  $\gamma$ -ray emission near IceCube-170922A is dominated at various times either by TXS 0506+056 or by PKS 0502+049 but there are also times when the two sources have roughly equal fluxes, as shown in Fig. 6.2. To investigate which of the sources dominate the  $\gamma$ -ray emission during the IceCube-170922A event and the neutrino flare period we constructed TS maps for

---

<sup>14</sup><http://openuniverse.asi.it>

<sup>15</sup>A fit to the SED around the time of the neutrino alert gives  $\nu_{peak}^S \sim 10^{15}$  Hz, making this an IBL/HBL source.

these two periods. We observe the following:

1. Fig. 6.3 shows the TS maps during the period contemporaneous with and before the IceCube-170922A event. From the maps it appears that TXS 0506+056 dominates the photon flux of the region at energies  $> 1 \text{ GeV}$ ;
2. during the time of the neutrino flare, on the other hand, the situation is different, with PKS 0502+049 being the brightest source at  $E > 1 \text{ GeV}$  and TXS 0506+056 progressively taking over above 2 and 5 GeV, as shown in Fig. 6.4.

We tried to unveil any evidence of  $\gamma$ -ray emission associated with the neighbour HBL 2WHSP J050833.3+05310, which is also within the 90 per cent error contour of IceCube-170922A, by conducting a series of eleven unbinned likelihood analyses, covering 9 years of observation with Fermi-LAT. We set energy cuts at  $E > 1 \text{ GeV}$  and  $> 5 \text{ GeV}$ , integrating over 400 days intervals<sup>16</sup>. We kept all 3FGL sources in the field, setting both normalizations and photon indexes as free parameters. At the 2WHSP J050833.3+05310 position an additional power-law source was included in the model. The strongest signature for  $\gamma$ -ray emission was found between MJD 55900 to 56300 for the 1 GeV energy cut, reaching  $\text{TS} \sim 5$ . This result was confirmed by the residual map of the region.

### 6.3.3 $\gamma$ -ray light curves

As discussed in Sect. 6.2.4, we have derived the  $\gamma$ -ray light and spectral index curves of TXS 0506+056 and PKS 0502+049. As inferred from Fig. 6.4, we have evidence that PKS 0502+049 dominates the  $\gamma$ -ray sky at low energies during the neutrino flare, possibly contaminating TXS 0506+056 below 2 GeV. We build the light curves for TXS 0506+056 integrating photons above 2 GeV to avoid any bias from PKS 0502+049 and also study the highest energies (above 10 GeV) during the specific neutrino flare period. This is the best compromise for the energy threshold. Ideally, one would like to sample as high energies as possible, to profit from the smaller Fermi-LAT PSF and source containment region and therefore reduce contamination from PKS 0502+049. However, the larger the energy, the smaller the photon statistics.

---

<sup>16</sup>Each bin has 100 days superposed to the previous/next bin, meaning we cover the following time windows: MJD 54700 to 55100, 55000 to 55400, 55300 to 55700... and so on.

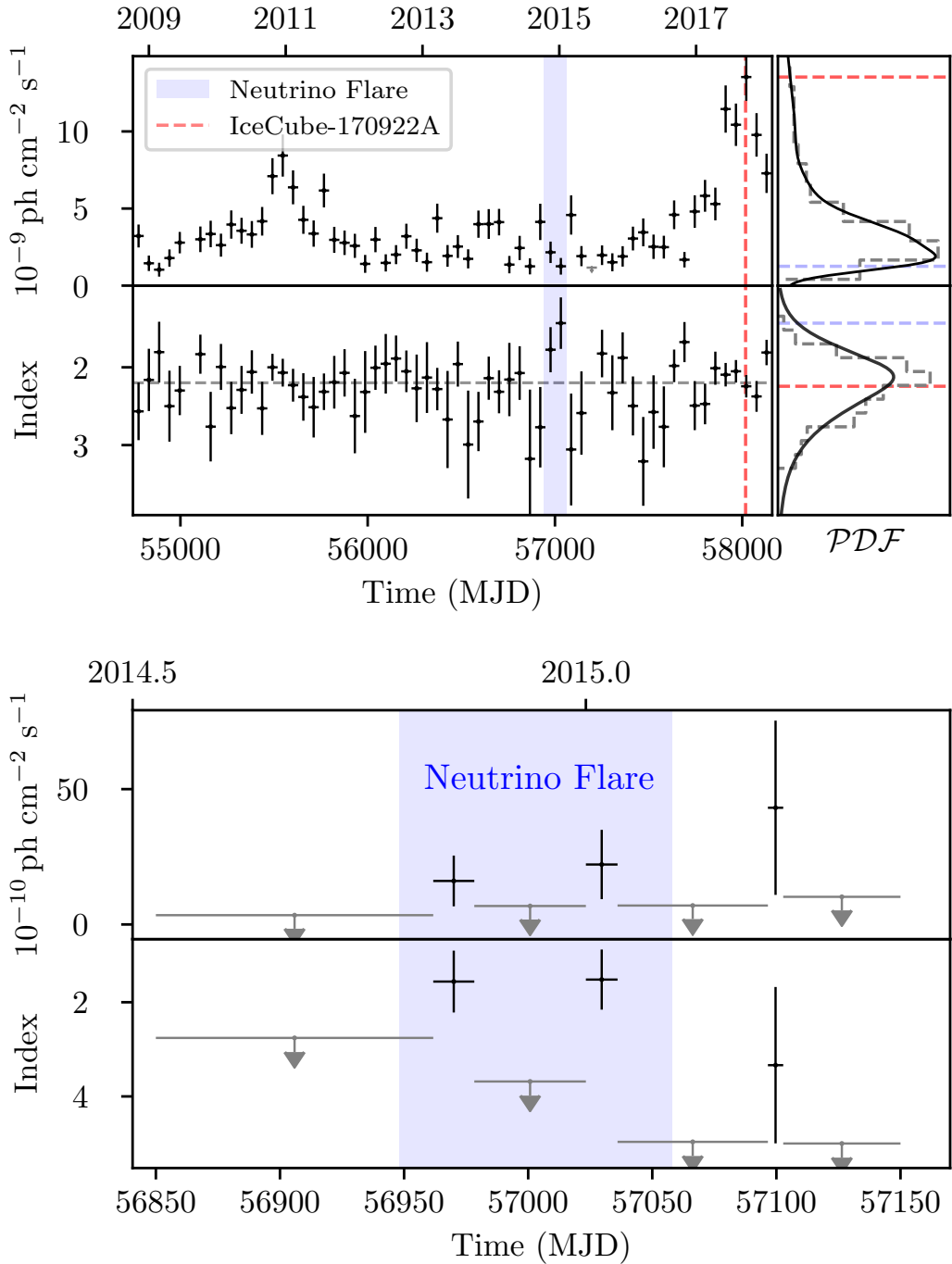


**Figure 6.5 Top:** light curve of TXS 0506+056 in 55-day bin at  $E > 2 \text{ GeV}$  and photon index curve. All points have a  $\text{TS} > 9$ , otherwise 95 per cent upper limits are shown. The blue band denotes the neutrino flare, while the red line indicates the IceCube-170922A event. The central horizontal line is the mean value of the spectral index. The corresponding photon flux and spectral index mean value distributions are shown as histograms (dashed grey) and kernel density estimations (solid black) in the top- and bottom-right panels respectively, with the values during the neutrino flare (blue) and the IceCube-170922A event (red) indicated as dashed lines. **Bottom:**  $\gamma$ -ray flux and photon index of TXS 0506+056 above 10 GeV, at the time of the neutrino excess observed around MJD 57000. The photon fluxes are calculated up to 300 GeV.

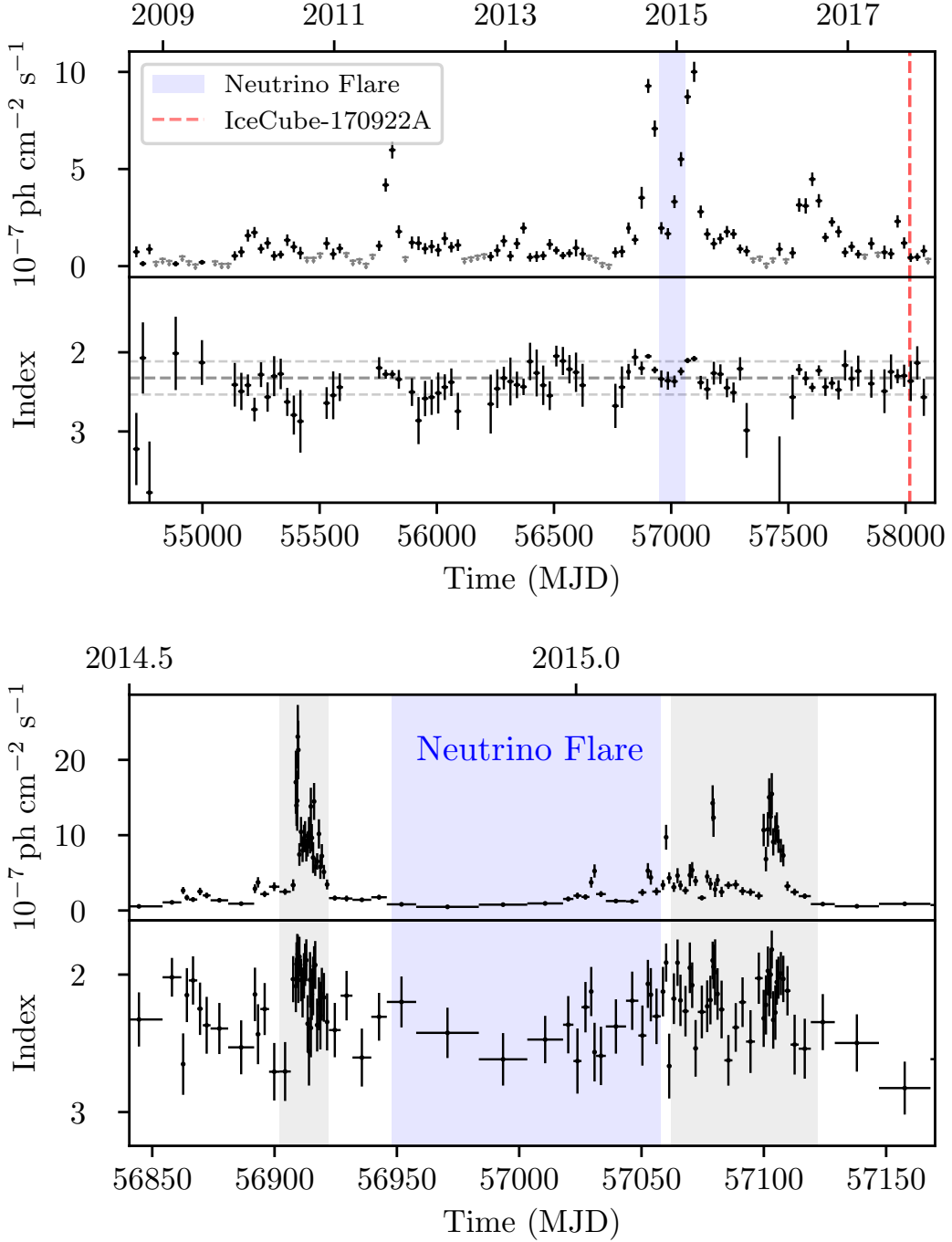


Figure 6.6 **Top:** light curve of PKS 0502+049 in 28-day bin and  $E > 0.1 \text{ GeV}$  and photon index curve. All points have a  $\text{TS} > 9$ , otherwise 95 per cent upper limits are shown. The blue band denotes the neutrino flare, while the red line indicates the IceCube-170922A event. The central horizontal line is the mean value of the spectral index. **Bottom:** adaptive bin light curve photon flux with  $E_{\min} = 214 \text{ MeV}$   $\gamma$ -ray light curve of PKS 0502+049 at the time of the neutrino excess observed around MJD 57000. The photon fluxes are calculated up to 300 GeV. The shaded bands at the left and right of the neutrino flare indicate the time windows where PKS 0502+049 is in a high photon flux state (see also Fig. 6.8).

In contrast, we build light curves for PKS 0502+049 above 0.1 GeV with fixed time bins and above 214 MeV with the adaptive binning method to study both long and short term structures. Fig. 6.5 (top) shows the light curve of TXS 0506+056. The blue band denotes the neutrino flare, while the red line indicates the IceCube-170922A event. Significant flux variations are visible, as typical of blazars. The corresponding photon flux and spectral index distributions are also shown on the right. It is interesting to note that TXS 0506+056 was at its hardest in the Fermi-LAT band during the neutrino flare, while being relatively faint (a “low/hard” state), and at its brightest during the IceCube-170922A event, while being softer (a “high/soft” state). Note that, based on the overall distributions, a spectral index as hard as observed during the neutrino flare is expected with a probability of only  $\sim 2$  per cent, while a flux as high at that during the IceCube-170922A event has a probability of only  $\sim 1$  per cent to be detected. The average photon index during the entire duration of the neutrino flare for  $E > 2$  GeV is  $1.62 \pm 0.20$ .

Since we want to concentrate on the highest energy photons we zoom in on the period around the neutrino flare to investigate in more detail the source variability looking for the most extreme emission using only events above 10 GeV. The period from MJD 56850 to MJD 56750 was then divided into half- and one-day bins and an unbinned maximum likelihood analysis was performed. Next, the nearby bins with  $TS > 0$  were merged and new light curves were calculated. In order to improve the statistics, the length of the time periods with  $TS > 0$  was then progressively increased by adding 1-hour intervals. As a result, we find two periods with significant emission above 10 GeV (Fig. 6.5, bottom): MJD 56961.75 – 56978.29 ( $TS = 30.5$ ), with the highest energy photon at 53.3 GeV, and MJD 57023.25 – 57036.0 ( $TS = 33.6$ ), with the highest energy photon at 52.6 GeV<sup>17</sup>.

Fig. 6.6 shows the light curve of PKS 0502+049. The blue band denotes the neutrino flare, while the red line indicates the IceCube-170922A event. Significant flux variations are also visible in this case in particular in the periods right before and after the neutrino flare but the overlap with the neutrino flare is minimal even taking into account the uncertainties on its duration as clearly visible in the adaptive bin zoom-in (see Fig. 6.6 bottom; the neutrino flare covers  $110^{+35}_{-24}$  days and we did not consider small  $\gamma$ -ray fluctuations over much shorter time scales). PKS 0502+049 presents no particular states in

---

<sup>17</sup>Based on the `gtsrcprob` tool both of these photons have a  $> 99$  per cent probability of being related to TXS 0506+056

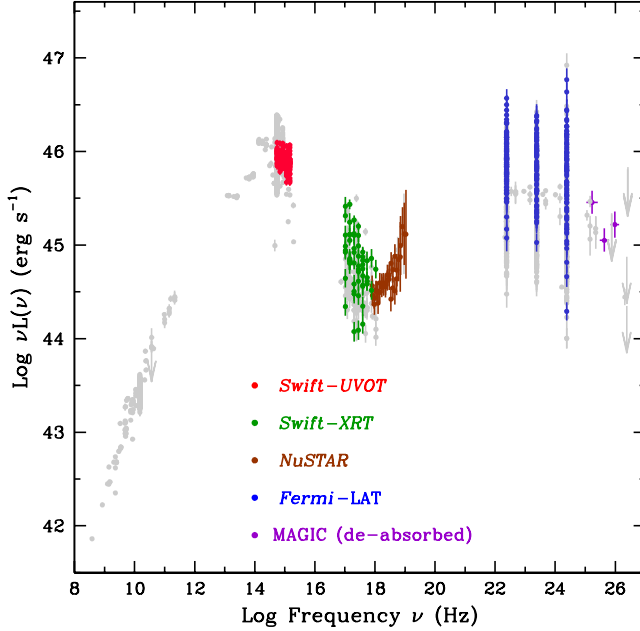


Figure 6.7 The SED of TXS 0506+056 assembled using all available public data. The blue measurements in the  $\gamma$ -ray band show the variability at 0.1, 1, and 10 GeV using Fermi-LAT data collected between January 1 and December 31, 2017 (see Fig. 6.10 for the 1 and 10 GeV light curves). Green and brown points at X-ray frequencies are from our analysis of Swift and NuSTAR data respectively. MAGIC data [184] are shown as purple crosses and were de-absorbed to correct for the extragalactic background light following [164]. Red points at optical and UV frequencies are from Swift-UVOT. The other non-simultaneous multi-frequency measurements are from catalogues and online archives (grey points).

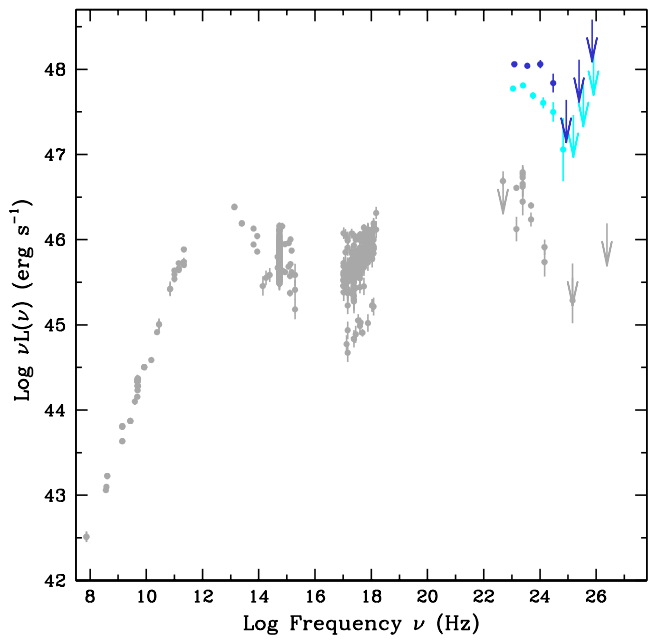


Figure 6.8 The SED of PKS 0502+049. The  $\gamma$ -ray spectra during the two flaring periods (see Fig. 6.6, bottom) are shown as blue (MJD 56902 – 56922) and cyan (MJD 57062 – 57122) points. All other multi-frequency data are non-simultaneous archival data.

photon flux and/or spectral index during IceCube-170922A and the neutrino flare period.

### 6.3.4 Spectral energy distributions

Fig. 6.7 shows the SED of TXS 0506+056. The NuSTAR data show a hardening at  $\sim 10^{18}$  Hz ( $\sim 4 - 5$  keV) most likely due to the onset of the inverse Compton component [e.g. 202]. Fig. 6.8 shows the SED of PKS 0502+049. Two points can be made: (1) during flares PKS 0502+049 is a brighter  $\gamma$ -ray source than TXS 0506+056; (2) the SED of PKS 0502+049 cuts off at  $E \approx 10$  GeV, while that of TXS 0506+056 reaches  $E \gtrsim 100$  GeV (compatibly with the likely extra-galactic background light absorption at its redshift: Paiano et al. 203).

To study the time evolution of the SED of TXS 0506+056 we have built an animation of nearly simultaneous data, which include 15 GHz monitoring data from OVRO, the ASAS  $V_{mag}$  light curve [189], the optical/UV data of the Swift-UVOT [207] analyzed with the SSDC online tool, and the X-ray and  $\gamma$ -ray data described in sect 6.2.3 and 6.2.4. The animation is available here: <https://youtu.be/lFBciGIT0mE>.

### The hybrid SED of TXS 0506+056

Fig. 6.9 shows the hybrid photon – neutrino SED of TXS 0506+056 for the period around the IceCube-170922A event (left) and the neutrino flare (right), based on the concept introduced by [199]. The red points are the electromagnetic emission simultaneous with the neutrinos. The detection of high-energy neutrinos above  $\sim 30$  TeV implies the existence of protons up to at least  $3 \times 10^{14} - 3 \times 10^{15}$  eV, which then collide with other protons ( $pp$  collisions) or photons ( $p\gamma$  collisions). High-energy  $\gamma$ -rays with energy and flux about a factor two higher than the neutrinos at the source are then expected as secondary products in both cases [187, 188]. Indeed, in both cases the (linearly extrapolated)  $\gamma$ -ray and neutrino fluxes are comparable, consistently with the hypothesis that they are produced by the same physical process. This is especially true for the neutrino flare, when the neutrino flux has a relatively small uncertainty being derived from  $\sim 13$  events within a well-defined period of  $110^{+35}_{-24}$  days [185].

This is different for the IceCube-170922A event, given the large uncertainty on the neutrino flux since we are dealing with a single event over an ill-defined period of time. To estimate the neutrino flux from one neutrino event

### 6.3 Putting it all together

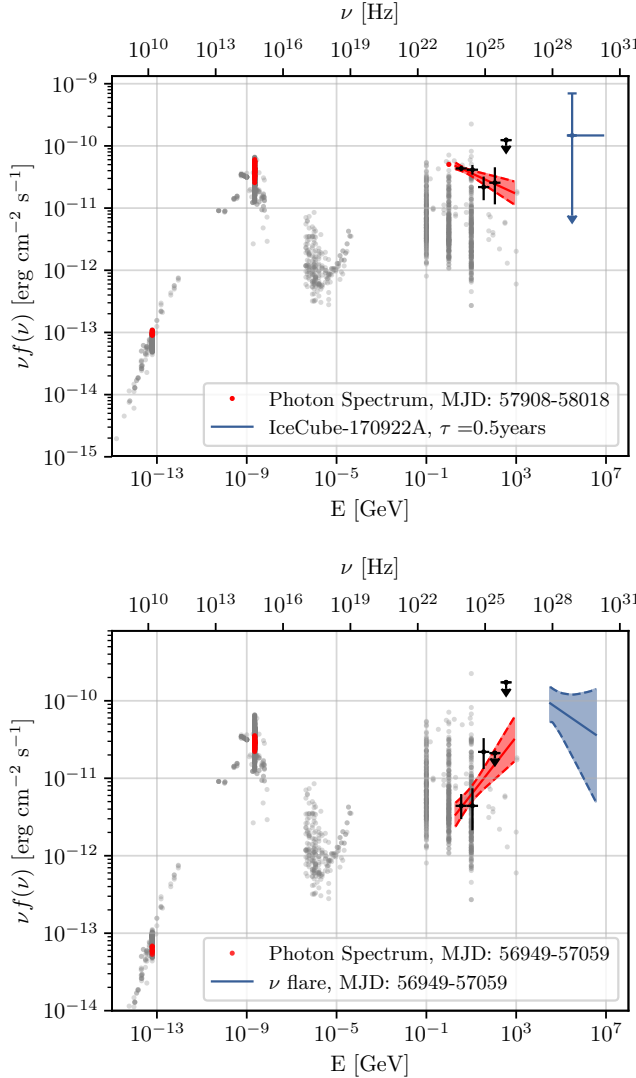


Figure 6.9 The hybrid photon – neutrino SED of TXS 0506+056. The red points (OVRO at 15 GHz and ASAS  $V_{mag}$ ) are simultaneous with neutrinos, grey ones refer to historical data, while the black ones are Fermi data. The red bands for the  $\gamma$ -ray flux show the  $1\sigma$  error bounds on the best fit, while upper limits are given at 95 per cent C.L.. Fermi data points were de-absorbed to correct for the extragalactic background light following [164]. **Left:** the MJD 57908 – 58018 period (June 4 – September 22, 2017). The neutrino flux has been derived by [184] over the 200 TeV – 7.5 PeV range (see text for more details); we give here the all-flavour flux. The vertical upper limit is drawn at the most probable neutrino energy. The average Fermi-LAT photon index for  $E > 2$  GeV is  $2.16 \pm 0.10$ . **Right:** the MJD 56949 – 57059 period (October 19, 2014 – February 6, 2015). The neutrino flux has been derived by [185] over the 32 TeV – 3.6 PeV range; the error is the combined error on the spectral index and the normalization. The average Fermi-LAT photon index for  $E > 2$  GeV is  $1.62 \pm 0.20$ .

[184] had to assume a spectral emission shape, an emission time  $\tau$ , and an energy emission range. The corresponding mean number of  $\nu_\mu$  events  $N$  expected in IceCube is

$$N = \tau \int_{E_{\min}}^{E_{\max}} A_{\text{eff}}(E, \theta) \cdot \frac{1}{3} \frac{d\phi}{dE} dE, \quad (6.3.1)$$

where  $A_{\text{eff}}$  is the effective area of the IceCube detector and  $\frac{1}{3}$  is the flavour ratio assumed. For a source described by a single power-law distribution the flux producing one neutrino event is

$$\phi_0 = \frac{3 \cdot N}{\tau \int_{E_{\min}}^{E_{\max}} A_{\text{eff}}(E, \theta) E^{-\gamma} dE}, \quad (6.3.2)$$

where  $N = 1$  and  $\tau$  is taken as 0.5 years (of the same order as the duration of the  $\gamma$ -ray flare). Interpreting the observation of one IceCube alert event as an upward Poissonian fluctuation, then the flux value calculated can be understood as an upper limit on the neutrino flux [see also 184].

## 6.4 Results

Following up the IceCube-170922A event observed in coincidence with a  $\gamma$ -ray flare of TXS 0506+056 [184], the IceCube collaboration has also detected a neutrino flare in late 2014 – early 2015 from the same direction [185]. Given the complexity of the  $\gamma$ -ray sky in this area, both spatially and temporally, we have carefully dissected the region and found the following:

1. out of the 637 radio and X-ray sources within 80 arc-minutes of the IceCube-170922A event position, only 7 are both radio and X-ray emitters and therefore likely non-thermal sources. As it turns out, the X-ray-to-radio flux ratios of these 7 sources are blazar-like;
2. out of these 7 sources, 4 are blazars, two of which are very bright  $\gamma$ -ray sources, namely TXS 0506+056 and PKS 0502+049, competing for dominance;

3. while TXS 0506+056 dominates in all  $\gamma$ -ray bands during the IceCube-170922A event, the situation is more complex during the neutrino flare, as PKS 0502+049 dominates up to  $E \sim 1 - 2$  GeV but TXS 0506+056 takes over at  $E \gtrsim 2 - 5$  GeV. The  $\gamma$ -ray spectrum of PKS 0502+049, in fact, cuts off at high energy even during flares, a behaviour typical of LBL blazars;
4. PKS 0502+049 is flaring right before and right after the neutrino flare (but not in coincidence with it) while TXS 0506+056 was at its hardest in that time period but in a relatively faint state, suggesting a shift to high energies of the  $\gamma$ -ray SED;
5. the hybrid  $\gamma$ -ray – neutrino SED of TXS 0506+056 during the neutrino flare is as expected for lepto-hadronic models since the photon and neutrino fluxes are at the same level [205]. We note that the hybrid SEDs of [199] and [201] were based on one shower-like IceCube event, which could in principle have been emitted over the full IceCube detection live time, and were therefore affected by a very large uncertainty. In the case of the neutrino flare, instead, a sizable ( $\sim 13$ ) number of neutrinos has been detected within a well-defined time window and good spatial resolution.

In short, all spatial, timing, and energetic multi-messenger diagnostics point to TXS 0506+056 as the first identified non-stellar neutrino (and therefore cosmic ray) source.

## 6.5 Discussion

### 6.5.1 Source properties

We now explore in more detail the properties of TXS 0506+056. First, we note that this source is a very strong  $\gamma$ -ray source, having an average flux of  $7.1 \times 10^{-8}$  ph cm $^{-2}$  s $^{-1}$  above 100 MeV, which puts it among the top 4 per cent of the Fermi 3LAC catalogue [153]. Moreover, it also belongs to the 2FHL sample [154], which includes all sources detected above 50 GeV by Fermi-LAT in 80 months of data. TXS 0506+056 also has a large radio flux density  $\sim 1$  Jy at 6 cm [173], and  $\sim 537$  mJy at 20 cm, which makes it one of the brightest radio sources (in the top 0.3 per cent) of the NRAO VLA Sky Survey,

which covers 82 per cent of the sky [163]. Fig. 6.7 shows the overall SED of the source in luminosity, based on the redshift of 0.3365 recently reported by [203].

The peak luminosities of  $\sim 2 \times 10^{46}$  erg s $^{-1}$  in the synchrotron peak, and almost  $10^{47}$  erg s $^{-1}$  at 10 GeV, place this object among the most powerful BL Lacs known, particularly in the high-energy/very high-energy  $\gamma$ -ray band. For comparison, the corresponding maximum luminosities ever observed in MKN 421 (and PKS 2155–304) are  $\sim 4 \times 10^{45}$  ( $\sim 2 \times 10^{46}$ ) and  $\sim 1.5 \times 10^{45}$  ( $10^{46}$ ) erg s $^{-1}$ , a factor of  $\sim 5$  (1) and  $\sim 50$  (10) lower than TXS 0506+056 (Giommi et al., in preparation). What seems to be peculiar in this source is the very large luminosity at  $\sim 10$  GeV compared to other similar sources. From the overall SED point of view TXS 0506+056 shows a variability range in the  $\gamma$ -ray band (almost a factor 1,000 at 10 GeV: see Fig. 6.7) much larger than that observed at the peak of the synchrotron emission. Even during the large  $\gamma$ -ray flaring event observed close to the detection of IceCube-170922A the peak of the synchrotron emission (located in the UV band) did not vary by more than a factor of 2, nor did the X-ray flux, at the tail of the synchrotron peak, change by a large factor. This behaviour is consistent with an excess of hard  $\gamma$ -ray radiation possibly associated with hadronic processes.

We now posses all the elements to calculate reliably the luminosity of a high-energy neutrino source. Using the fluence, spectral index, and energy range given in Sect. 6.2.1 and [185] we do the following: 1. derive an integrated  $\nu_\mu$  flux of  $1.2 \times 10^{-10}$  erg cm $^{-2}$  s $^{-1}$  from the fluence by integrating over the  $2\sigma$  range around the central value of the time period; 2. estimate  $L_{\nu_\mu}$ ; 3. derive a neutrino luminosity all-flavour (assuming  $\nu_e : \nu_\mu : \nu_\tau = 1 : 1 : 1$ ) by multiplying by 3 the  $\nu_\mu$  power. The result is  $L_\nu = 3 \times L_{\nu_\mu} \sim 3 \times 4.5 \times 10^{46}$  erg s $^{-1} \sim 1.4_{-0.5}^{+0.6} \times 10^{47}$  erg s $^{-1}$  between 32 TeV and 3.6 PeV. (This luminosity is fully consistent with the one derived by [185] of  $1.2_{-0.4}^{+0.6} \times 10^{47}$  erg s $^{-1}$  based on a flare duration of 158 days derived from the box time-window result.)

This can be compared to the simultaneous  $\gamma$ -ray luminosity  $L_\gamma$  (2 GeV – 1 TeV)<sup>18</sup>  $\sim 3 \times 10^{46}$  erg s $^{-1}$  [or  $L_\gamma$  (2 GeV – 100 GeV)  $\sim 10^{46}$  erg s $^{-1}$ ].

### 6.5.2 Physical implications

Our results have several physical implications. Namely:

---

<sup>18</sup>This is based on the Fermi-LAT best fit extrapolated to 1 TeV.

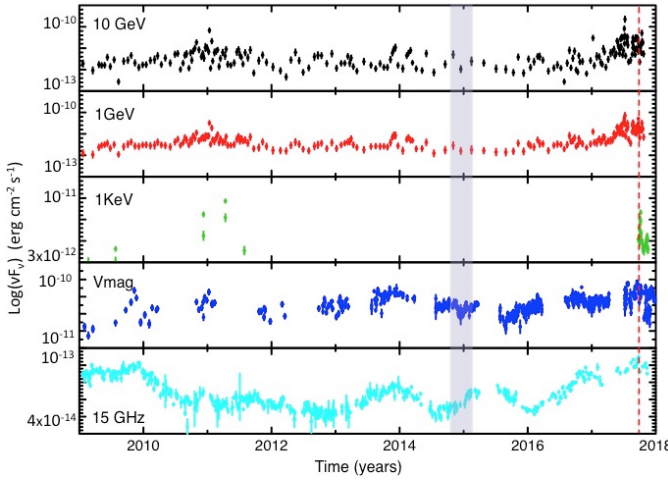


Figure 6.10 The radio (15 GHz), optical ( $V_{mag}$ ), X-ray and  $\gamma$ -ray light curves of TXS 0506+056. The radio data have been taken from the OVRO database, the visual magnitude data are from the Catalina Real Time Transient Survey (CRTS) and from the All Sky Automatic Survey ASAS [189]. The  $\gamma$ -ray light curves have been produced using Fermi-LAT data with the adaptive-bin method [191]. The blue band denotes the neutrino flare, while the red line indicates the IceCube-170922A event.

## *6 Dissecting the region around IceCube-170922A: the blazar TXS 0506+056 as the first cosmic neutrino source*

---

1. with neutrinos we are exploring an energy range which is inaccessible with photons at this redshift. Therefore, the first evidence for neutrino emission from the direction of TXS 0506+056 opens a new window on blazar physics;
2. the derived  $L_\nu$  during the neutrino flare is quite large and even larger than  $L_\gamma$  (2 GeV – 1 TeV), which might imply that a sizeable fraction of the neutrino-related  $\gamma$ -rays have energies above the Fermi-LAT energy band, as expected in the case of  $p\gamma$  collisions (Sect. 6.3.4);
3. the ratio between the two SED humps (high-energy to low-energy, usually known as Compton dominance [CD]: e.g. Giommi et al. 169) for TXS 0506+056 is  $> 1$ , while typical HBL have  $CD \sim 0.1$ . This could be due to the electromagnetic emission coming from different blobs e.g. one dominant at optical frequencies and the other dominant at high-energy  $\gamma$ -rays, or to the presence of an additional hadronic component in the  $\gamma$ -ray band;
4. a discrete cross-correlation analysis using the z-transformed discrete correlation function [ZDCF; 156] among the radio (15 GHz), optical, X-ray and  $\gamma$ -ray light curves of TXS 0506+056, was built with the data described in the previous paragraphs (Fig. 6.10). The ZDCF shows a strong correlation ( $\sim 10\sigma$ ) with a time lag of  $\approx 4$  months between the radio and optical emission (with the optical band leading) but no correlation between optical/X-ray/radio and  $\gamma$ -ray bands. This is at variance with typical single-zone leptonic (synchrotron self-Compton or external Compton) models where all energy bands are expected to be well correlated;
5. the SED of at least one blazar now has to be modeled within a leptohadronic scenario [e.g. 205]. This is far from trivial and goes well beyond the scope of this paper;
6. the neutrino sky has been populated so far by only two sources: the Sun [e.g. 160] and SN 1987A [176, 159, 157]. TXS 0506+056 is now a third plausible candidate, whose neutrino energies are, however, more than six orders of magnitude larger than those of the two stellar sources.

### 6.5.3 Future searches

Our results suggest two periods of neutrino emission for TXS 0506+056, which appear to be in connection with two very different  $\gamma$ -ray states, namely one high/soft, connected to the IceCube-170922A event, and another one low/hard, related to the neutrino flare. This implies that the search for multi-messenger sources needs to be carried out not only for flaring  $\gamma$ -ray sources but also for relatively hard emitters. These criteria can also be used by neutrino telescopes to look for other neutrino sources.

Why is this the only strong IceCube neutrino source candidate? What makes it special? We believe this is due to a series of factors. First, as discussed in Sect. 6.5.1, TXS 0506+056 is a very strong  $\gamma$ -ray and radio source. Moreover, its declination and energy range happened to be in the regions of parameter space where IceCube reaches maximum sensitivity and the duration of the flare was also long enough for IceCube to (marginally) detect it (see also IceCube Collaboration 185).

Future searches for cosmic neutrino sources should emphasize: (1) extreme blazars of the BL Lac type, as hinted at by [201]; (2) high/soft – low/hard  $\gamma$ -ray states; (3) regions of parameter space where the neutrino detectors are most sensitive.

## 6.6 Conclusions

The IceCube-170922A event and the neutrino flare at the end of 2014 have been linked to the same source, TXS 0506+056, a blazar of the BL Lac type at  $z = 0.3365$ . This is the most plausible association so far between IceCube neutrinos and an extragalactic object. The area near TXS 0506+056 is quite complex due to the presence of several non- thermal sources, which in principle could all contribute to the overall  $\gamma$ -ray flux. We have therefore carefully dissected this region using a multi-messenger approach, obtaining the following results:

1. TXS 0506+056 was the brightest Fermi source in the region of interest at energies above 1 GeV during the IceCube-170922A event but only above 2 – 5 GeV during the neutrino flare. PKS 0502+049, a nearby blazar of the FSRQ type offset by  $\sim 1.2^\circ$ , dominated the  $\gamma$ -ray region at lower energies in the latter period.

## *6 Dissecting the region around IceCube-170922A: the blazar TXS 0506+056 as the first cosmic neutrino source*

---

2. We have observed two periods of significant neutrino emission consistent with the position of TXS 0506+056 in connection with two very different  $\gamma$ -ray states, namely one, high/soft, connected to the IceCube-170922A event, and another one, low/hard, related to the neutrino flare. PKS 0502+049 was also flaring right before and right after the neutrino flare but not in coincidence with it.
3. We have built the hybrid photon – neutrino SED of TXS 0506+056 during the neutrino flare and have reliably estimated the power of a high-energy neutrino source. This is  $\sim 1.4 \times 10^{47}$  erg s $^{-1}$  between 32 TeV and 3.6 PeV (all-flavour), even larger than the simultaneous  $L_\gamma$  (2 GeV – 1 TeV)  $\sim 3 \times 10^{46}$  erg s $^{-1}$ .
4. Both the lack of a correlation between the  $\gamma$ -ray and radio/optical flux and the SED shape of TXS 0506+056, which is unusual in terms of its Compton dominance, appear not to be consistent with simple leptonic models.
5. All of the above is fully consistent with the hypothesis that TXS 0506+056 has undergone a hadronic flare during the neutrino detections.

In short, all spatial, timing, and energetic multi-messenger diagnostics point to TXS 0506+056 as the only counterpart of all the neutrinos observed in the vicinity of IceCube-170922A and therefore the first non-stellar neutrino (and hence cosmic ray) source. The emergent picture is that extreme blazars, i.e., strong, very high energy  $\gamma$ -ray sources with the peak of the synchrotron emission  $> 10^{14} - 10^{15}$  Hz [201], are the first class of sources with evident contribution to the IceCube diffuse signal [181, 182].

Future searches for cosmic neutrino sources, concentrated on similar classes of sources, using additional high-energy track-like events, and based on detailed multi-messenger analysis, will likely provide further associations.

# Bibliography

- [1] Aartsen, M. G., Abraham, K., Ackermann, M., & et al. 2017, *ApJ*, 835, 151
- [2] —. 2017, *ApJ*, 835, 45
- [3] Aartsen, M. G., Abbasi, R., Abdou, Y., et al. 2013, *Physical Review Letters*, 111, 021103
- [4] Aartsen, M. G., Ackermann, M., Adams, J., et al. 2014, *Physical Review Letters*, 113, 101101
- [5] Aharonian, F. A. 2000, *NewA*, 5, 377
- [6] Aharonian, F. A., Barkov, M. V., & Khangulyan, D. 2017, *ApJ*, 841, 61
- [7] Aharonian, F. A., Belyanin, A. A., Derishev, E. V., Kocharovsky, V. V., & Kocharovsky, V. V. 2002, *Phys. Rev. D*, 66, 023005
- [8] Ahnen, M. L., Ansoldi, S., Antonelli, L. A., et al. 2018, *ArXiv e-prints*, arXiv:1807.04300
- [9] Araudo, A. T., Bosch-Ramon, V., & Romero, G. E. 2010, *A&A*, 522, A97
- [10] —. 2013, *MNRAS*, 436, 3626
- [11] Barkov, M. V., Aharonian, F. A., Bogovalov, S. V., Kelner, S. R., & Khangulyan, D. 2012, *ApJ*, 749, 119
- [12] Barkov, M. V., Aharonian, F. A., & Bosch-Ramon, V. 2010, *ApJ*, 724, 1517
- [13] Barkov, M. V., Bosch-Ramon, V., & Aharonian, F. A. 2012, *ApJ*, 755, 170
- [14] Beall, J. H., & Bednarek, W. 1999, *ApJ*, 510, 188
- [15] Bednarek, W. 2016, *ApJ*, 833, 279
- [16] Bednarek, W., & Banasiński, P. 2015, *ApJ*, 807, 168

## *Bibliography*

---

- [17] Bednarek, W., & Protheroe, R. J. 1997, MNRAS, 287, L9
- [18] Berezinskii, V. S., Bulanov, S. V., Dogiel, V. A., & Ptuskin, V. S. 1990, Astrophysics of cosmic rays
- [84] Błażejowski, M., Sikora, M., Moderski, R., & Madejski, G. M. 2000, ApJ, 545, 107
- [85] Bloom, S. D., & Marscher, A. P. 1996, ApJ, 461, 657
- [21] Bosch-Ramon, V., Perucho, M., & Barkov, M. V. 2012, A&A, 539, A69
- [22] Böttcher, M., & Dermer, C. D. 2010, ApJ, 711, 445
- [23] Dar, A., & Laor, A. 1997, ApJL, 478, L5
- [24] de la Cita, V. M., Bosch-Ramon, V., Paredes-Fortuny, X., Khangulyan, D., & Perucho, M. 2016, A&A, 591, A15
- [25] Domínguez, A., Primack, J. R., Rosario, D. J., et al. 2011, MNRAS, 410, 2556
- [26] Georganopoulos, M., & Kazanas, D. 2003, ApJL, 594, L27
- [103] Ghisellini, G., Maraschi, L., & Treves, A. 1985, A&A, 146, 204
- [104] Ghisellini, G., & Tavecchio, F. 2009, MNRAS, 397, 985
- [105] —. 2015, MNRAS, 448, 1060
- [30] Giannios, D., Uzdensky, D. A., & Begelman, M. C. 2009, MNRAS, 395, L29
- [31] —. 2010, MNRAS, 402, 1649
- [32] IceCube, T., Fermi-LAT, MAGIC, et al. 2018, ArXiv e-prints, arXiv:1807.08816
- [33] IceCube Collaboration. 2013, Science, 342, 1242856
- [34] —. 2018, ArXiv e-prints, arXiv:1807.08794
- [35] Inoue, S., & Takahara, F. 1996, ApJ, 463, 555

---

## Bibliography

- [36] Joshi, M., & Böttcher, M. 2011, *ApJ*, 727, 21
- [37] Kadler, M., Krauß, F., Mannheim, K., & et al. 2016, *Nature Physics*, 12, 807
- [38] Kappes, A., Hinton, J., Stegmann, C., & Aharonian, F. A. 2007, *ApJ*, 656, 870
- [39] Keivani, A., Murase, K., Petropoulou, M., et al. 2018, ArXiv e-prints, arXiv:1807.04537
- [40] Kelner, S. R., Aharonian, F. A., & Bugayov, V. V. 2006, *Phys. Rev. D*, 74, 034018
- [41] Khangulyan, D. V., Barkov, M. V., Bosch-Ramon, V., Aharonian, F. A., & Dorodnitsyn, A. V. 2013, *ApJ*, 774, 113
- [42] Khiali, B., & de Gouveia Dal Pino, E. M. 2016, *MNRAS*, 455, 838
- [43] Mannheim, K. 1995, *Astroparticle Physics*, 3, 295
- [44] Mannheim, K., & Biermann, P. L. 1992, *A&A*, 253, L21
- [45] Maraschi, L., Ghisellini, G., & Celotti, A. 1992, *ApJL*, 397, L5
- [46] Marscher, A. P., & Gear, W. K. 1985, *ApJ*, 298, 114
- [47] Mücke, A., & Protheroe, R. J. 2001, *Astroparticle Physics*, 15, 121
- [48] Murase, K., Guetta, D., & Ahlers, M. 2016, *Physical Review Letters*, 116, 071101
- [49] Netzer, H. 2015, *ARA& A*, 53, 365
- [50] Padovani, P., Giommi, P., Resconi, E., et al. 2018, ArXiv e-prints, arXiv:1807.04461
- [51] Padovani, P., & Resconi, E. 2014, *Monthly Notices of the Royal Astronomical Society*, 443, 474
- [52] Padovani, P., Resconi, E., Giommi, P., Arsioli, B., & Chang, Y. L. 2016, *Monthly Notices of the Royal Astronomical Society*, 457, 3582

## Bibliography

---

- [53] Paiano, S., Falomo, R., Treves, A., & Scarpa, R. 2018, ApJL, 854, L32
- [54] Perucho, M., Bosch-Ramon, V., & Barkov, M. V. 2017, A&A, 606, A40
- [55] Peterson, B. M. 2006, in Lecture Notes in Physics, Berlin Springer Verlag, Vol. 693, Physics of Active Galactic Nuclei at all Scales, ed. D. Alloin, 77
- [56] Protheroe, R. J. 1997, in Astronomical Society of the Pacific Conference Series, Vol. 121, IAU Colloq. 163: Accretion Phenomena and Related Outflows, ed. D. T. Wickramasinghe, G. V. Bicknell, & L. Ferrario, 585
- [57] Sahakyan, N., Piano, G., & Tavani, M. 2014, ApJ, 780, 29
- [139] Sikora, M., Begelman, M. C., & Rees, M. J. 1994, ApJ, 421, 153
- [140] Sikora, M., Stawarz, Ł., Moderski, R., Nalewajko, K., & Madejski, G. M. 2009, ApJ, 704, 38
- [60] Sokolov, A., Marscher, A. P., & McHardy, I. M. 2004, ApJ, 613, 725
- [61] Spada, M., Ghisellini, G., Lazzati, D., & Celotti, A. 2001, MNRAS, 325, 1559
- [62] Tavecchio, F., & Ghisellini, G. 2008, MNRAS, 385, L98
- [63] —. 2015, MNRAS, 451, 1502
- [142] Urry, C. M., & Padovani, P. 1995, PASP, 107, 803
- [65] Wang, X.-Y., & Liu, R.-Y. 2016, Phys. Rev. D, 93, 083005
- [66] Yoshida, S., Dai, H., Jui, C. C. H., & Sommers, P. 1997, ApJ, 479, 547
- [146] Zabalza, V. 2015, in International Cosmic Ray Conference, Vol. 34, 34th International Cosmic Ray Conference (ICRC2015), 922
- [68] Abdo, A. A., Ackermann, M., Ajello, M., & et al. 2010, ApJ, 722, 520
- [69] Abdo, A. A., Ackermann, M., Ajello, M., & et al. 2011, ApJL, 733, L26
- [70] Abdo, A. A., Ackermann, M., Agudo, I., et al. 2010, ApJ, 721, 1425
- [71] Abdo, A. A., Ackermann, M., Ajello, M., et al. 2010, ApJL, 714, L73

---

## Bibliography

- [72] —. 2010, *ApJ*, 710, 810
- [73] —. 2010, *ApJ*, 710, 1271
- [74] Acero, F., Ackermann, M., Ajello, M., & et al. 2015, *ApJSS*, 218, 23
- [75] Ackermann, M., Ajello, M., & et al. 2015, *ApJ*, 810, 14
- [76] Ackermann, M., Anantua, R., & et al. 2016, *ApJL*, 824, L20
- [77] Ackermann, M., Ajello, M., Baldini, L., et al. 2010, *ApJ*, 721, 1383
- [78] Ahnen, M. L., Ansoldi, S., & et al. 2015, *ApJL*, 815, L23
- [79] Aleksić, J., Ansoldi, S., & et al. 2014, *A&A*, 569, A46
- [80] Aleksić, J., Antonelli, L. A., & et al. 2011, *ApJL*, 730, L8
- [81] Baghmanyan, V., Gasparyan, S., & Sahakyan, N. 2017, *ApJ*, 848, 111
- [82] Balonek, T. J., Zhang, S., & et al. 2016, *The Astronomer's Telegram*, 9732
- [83] Becerra, J., Carpenter, B., & Cutini, S. 2016, *The Astronomer's Telegram*, 8722
- [84] Błażejowski, M., Sikora, M., Moderski, R., & Madejski, G. M. 2000, *ApJ*, 545, 107
- [85] Bloom, S. D., & Marscher, A. P. 1996, *ApJ*, 461, 657
- [86] Breeveld, A. A., Landsman, W., Holland, S. T., et al. 2011, in American Institute of Physics Conference Series, Vol. 1358, , 373–376
- [87] Brown, A. M. 2013, *MNRAS*, 431, 824
- [88] Bulgarelli, A., Verrecchia, F., & et al. 2016, *The Astronomer's Telegram*, 9788
- [89] Carrasco, L., Miramon, J., Recillas, E., et al. 2016, *The Astronomer's Telegram*, 8574
- [90] Casadio, C., Gómez, J. L., & et al. 2015, *ApJ*, 813, 51
- [91] Cash, W. 1979, *ApJ*, 228, 939

## *Bibliography*

---

- [92] Celotti, A., & Ghisellini, G. 2008, MNRAS, 385, 283
- [93] —. 2008, MNRAS, 385, 283
- [94] Chapman, K. J., Sabyr, A., Stahlin, R. W., Zhang, S., & Balonek, T. J. 2016, The Astronomer's Telegram, 9756
- [95] Ciprini, S. 2016, The Astronomer's Telegram, 9869
- [96] —. 2017, The Astronomer's Telegram, 10292
- [97] D'Ammando, F., Raiteri, C. M., Villata, M., et al. 2011, A&A, 529, A145
- [98] Elliot, J. L., & Shapiro, S. L. 1974, ApJL, 192, L3
- [99] Fitzpatrick, E. L. 1999, , 111, 63
- [100] Foschini, L., Bonnoli, G., Ghisellini, G., et al. 2013, A&A, 555, A138
- [101] Foschini, L., Ghisellini, G., Tavecchio, F., Bonnoli, G., & Stamerra, A. 2011, A&A, 530, A77
- [102] Ghisellini, G., Maraschi, L., & Tavecchio, F. 2009, MNRAS, 396, L105
- [103] Ghisellini, G., Maraschi, L., & Treves, A. 1985, A&A, 146, 204
- [104] Ghisellini, G., & Tavecchio, F. 2009, MNRAS, 397, 985
- [105] —. 2015, MNRAS, 448, 1060
- [106] Ghisellini, G., Tavecchio, F., & et al. 2014, Nature, 515, 376
- [107] Ghisellini, G., Tavecchio, F., Foschini, L., & Ghirlanda, G. 2011, MNRAS, 414, 2674
- [108] Harrison, F. A., Craig, W. W., Christensen, F. E., & et al. 2013, ApJ, 770, 103
- [109] Hayashida, M., Nalewajko, K., & et al. 2015, ApJ, 807, 79
- [110] Kataoka, J., Madejski, G., Sikora, M., et al. 2008, ApJ, 672, 787
- [111] Kirk, J. G., Rieger, F. M., & Mastichiadis, A. 1998, A&A, 333, 452

---

## Bibliography

- [112] Liu, H. T., & Bai, J. M. 2006, *ApJ*, 653, 1089
- [113] Lott, B., Escande, L., Larsson, S., & Ballet, J. 2012, *A&A*, 544, A6
- [114] Malmrose, M. P., Marscher, A. P., Jorstad, S. G., Nikutta, R., & Elitzur, M. 2011, *ApJ*, 732, 116
- [115] Maraschi, L., Ghisellini, G., & Celotti, A. 1992, *ApJL*, 397, L5
- [116] Massaro, E., Perri, M., Giommi, P., & Nesci, R. 2004, *A&A*, 413, 489
- [117] Massaro, F., & D'Abrusco, R. 2016, *ApJ*, 827, 67
- [118] Minervini, G., Piano, G., & et al. 2016, *The Astronomer's Telegram*, 9743
- [119] Moore, R. L., & Stockman, H. S. 1981, *ApJ*, 243, 60
- [120] Mücke, A., & Protheroe, R. J. 2001, *Astroparticle Physics*, 15, 121
- [121] Mücke, A., Protheroe, R. J., Engel, R., Rachen, J. P., & Stanev, T. 2003, *Astroparticle Physics*, 18, 593
- [122] Nalewajko, K. 2013, *MNRAS*, 430, 1324
- [123] Nenkova, M., Sirocky, M. M., Nikutta, R., Ivezić, Ž., & Elitzur, M. 2008, *ApJ*, 685, 160
- [124] Paggi, A., Cavaliere, A., Vittorini, V., D'Ammando, F., & Tavani, M. 2011, *ApJ*, 736, 128
- [125] Pian, E., Falomo, R., & Treves, A. 2005, *MNRAS*, 361, 919
- [126] Pica, A. J., Smith, A. G., Webb, J. R., et al. 1988, *AJ*, 96, 1215
- [127] Popov, V., & Bachev, R. 2016, *The Astronomer's Telegram*, 9776
- [128] Poutanen, J., & Stern, B. 2010, *ApJL*, 717, L118
- [129] —. 2010, *ApJL*, 717, L118
- [130] Raiteri, C. M., Villata, M., Acosta-Pulido, J. A., et al. 2017, *Nature*, 552, 374

## Bibliography

---

- [131] Rani, B., Lott, B., Krichbaum, T. P., Fuhrmann, L., & Zensus, J. A. 2013, *A&A*, 557, A71
- [132] Rybicki, G. B., & Lightman, A. P. 1979, Radiative processes in astrophysics
- [133] Sahakyan, N., & Gasparyan, S. 2017, *MNRAS*, 470, 2861
- [134] Saito, S., Stawarz, Ł., & et al. 2013, *ApJL*, 766, L11
- [135] Sbarrato, T., Ghisellini, G., Maraschi, L., & Colpi, M. 2012, *MNRAS*, 421, 1764
- [136] Schlaufly, E. F., & Finkbeiner, D. P. 2011, *ApJ*, 737, 103
- [137] Schmidt, M. 1965, *ApJ*, 141, 1295
- [138] Shukla, A., Mannheim, K., Patel, S. R., et al. 2018, *ApJL*, 854, L26
- [139] Sikora, M., Begelman, M. C., & Rees, M. J. 1994, *ApJ*, 421, 153
- [140] Sikora, M., Stawarz, Ł., Moderski, R., Nalewajko, K., & Madejski, G. M. 2009, *ApJ*, 704, 38
- [141] Tavecchio, F., Becerra-Gonzalez, J., Ghisellini, G., et al. 2011, *A&A*, 534, A86
- [142] Urry, C. M., & Padovani, P. 1995, , 107, 803
- [143] Vaughan, S., Edelson, R., Warwick, R. S., & Uttley, P. 2003, *MNRAS*, 345, 1271
- [144] Vercellone, S., D’Ammando, F., Vittorini, V., et al. 2010, *ApJ*, 712, 405
- [145] Vercellone, S., Striani, E., Vittorini, V., et al. 2011, *ApJL*, 736, L38
- [146] Zabalza, V. 2015, Proc. of International Cosmic Ray Conference 2015, in press
- [147] Aartsen M. G., et al., 2013, *Phys. Rev. Lett.*, 111, 021103
- [148] Aartsen M. G., et al., 2015, *Phys. Rev. Lett.*, 115, 081102
- [149] Aartsen M. G., et al., 2016, *ApJ*, 833, 3

---

## Bibliography

- [150] Aartsen M. G., et al., 2017, *ApJ*, 835, 45
- [151] Acero, F., Ackermann, M., Ajello, M., et al. 2015, *ApJSS*, 218, 23
- [152] Ackermann M., et al., 2011, *ApJ*, 743, 171
- [153] Ackermann M., et al., 2015, *ApJ*, 810, 14
- [154] Ackermann M., et al., 2016, *ApJS*, 222, 5
- [155] Ahlers M., Halzen F., 2015, *Rep. Prog. Phys.*, 78, 126901
- [156] Alexander T., 1997, *Astrophysics and Space Science Library* Vol. 218, 163
- [157] Alekseev E. N., Alekseeva L. N., Volchenko V. I., Krivosheina I. V., 1987, *PZETF*, 45, 461
- [158] Atwood W. B., et al., 2009, *ApJ*, 697, 1071
- [159] Bionta R. M., et al., 1987, *PhRvL*, 58, 1494
- [160] BOREXINO Collaboration, et al., 2014, *Nature*, 512, 383
- [161] Burrows D., et al. 2005, *Space Science Rev.* 120, 165
- [162] Chang Y.L., Arsioli B., Giommi P. & Padovani P., 2017, *A&A*, 598, 17
- [163] Condon J. J., Cotton W. D., Greisen E. W., Yin Q. F., Perley R. A., Taylor G. B., Broderick J. J., 1998, *AJ*, 115, 1693
- [164] Domínguez A., et al., 2011, *MNRAS*, 410, 2556
- [165] Fiore F., et al., 2017, *A&A*, 601, A143
- [166] Gehrels N. et al. 2004, *ApJ*, 611, 1005
- [167] Ghisellini G., Righi C., Costamante L., Tavecchio F., 2017, *MNRAS*, 469, 255
- [168] Giommi P., Padovani P., Polenta G., Turriziani S., D'Elia V., Piranomonte S., 2012a, *MNRAS*, 420, 2899
- [169] Giommi P. et al., 2012b, *A&A* 541, 160

## *Bibliography*

---

- [170] Giommi P., 2015, JHEAp, 7, 173
- [171] Giommi P., Padovani P. & Polenta G., 2013, MNRAS, 431, 1914.
- [172] Giommi P., Padovani P., 2015, MNRAS, 450, 2404
- [173] Gregory P. C., Condon J. J., 1991, ApJS, 75, 1011
- [174] Halzen F., Zas E., 1997, ApJ, 488, 669
- [175] Harrison F., et al., 2013 ApJ, 770, 103
- [176] Hirata K., et al., 1987, PhRvL, 58, 1490
- [177] IceCube Collaboration, 2013, Science, 342, 1242856
- [178] IceCube Collaboration, 2014, Phys. Rev. Lett., 113, 101101
- [179] IceCube Collaboration, 2015a, Contributions to the 34th International Cosmic Ray Conference (ICRC 2015), p. 45 (arXiv:1510.05223)
- [180] IceCube Collaboration, 2015b, Contributions to the 34th International Cosmic Ray Conference (ICRC 2015), p. 37 (arXiv:1510.05223)
- [181] IceCube Collaboration, 2017a, Contributions to the 35th International Cosmic Ray Conference (ICRC 2017), p. 30 (arXiv:1710.01191)
- [182] IceCube Collaboration, 2017b, Contributions to the 35th International Cosmic Ray Conference (ICRC 2017), p. 54 (arXiv:1710.01191)
- [183] IceCube Collaboration, 2017c, Contributions to the 35th International Cosmic Ray Conference (ICRC 2017), p. 31 (arXiv:1710.01179)
- [184] IceCube Collaboration, 2018a, Science, submitted
- [185] IceCube Collaboration, 2018b, Science, submitted
- [186] Keivani A., et al., 2017, GCN, 21930, 1
- [187] Kelner S. R., Aharonian F. A., Bugayov V. V., 2006, Phys. Rev. D, 74, 034018
- [188] Kelner S. R., Aharonian F. A., 2008, Phys. Rev. D, 78, 034013

---

## Bibliography

- [189] Kochanek, C. S. et al. 2017, PASP, 129, 4502
- [190] Kopper C., Blaufuss E., 2017, GCN, 21916, 1
- [191] Lott B., Escande L., Larsson S., Ballet J., 2012, A&A, 544, A6
- [192] Lucarelli F., et al., 2017a, ApJ, 846, 121
- [193] Lucarelli F., et al., 2017b, ATel, 10801
- [194] Mannheim K., 1995, Astroparticle Physics, 3, 295
- [195] Massaro E., et al. 2015, Ap&SS 357, 75
- [196] Mattox, J. R., Bertsch, D. L., Chiang, J., et al. 1996, ApJ, 461, 396
- [197] Mücke A. et al., 2003, Astroparticle Physics, 18, 593
- [198] Padovani P., Giommi P., 1995, ApJ, 444, 567
- [199] Padovani P., Resconi E., 2014, MNRAS, 443, 474 (PR14)
- [200] Padovani P., Giommi P., 2015, MNRAS, 446, L41
- [201] Padovani P., Resconi E., Giommi P., Arsioli B., Chang Y. L., 2016, MNRAS, 457, 3582
- [202] Padovani P., et al., 2017, A&ARv, 25, 2
- [203] Paiano S., Falomo R., Treves A., Scarpa R., 2018, ApJ, 854, L32
- [204] Palladino A., Vissani F., 2017, A&A, 604, A18
- [205] Petropoulou M., Dimitrakoudis S., Padovani P., Mastichiadis A., Resconi E., 2015, MNRAS, 448, 2412
- [206] Resconi E., Coenders S., Padovani P., Giommi P., Caccianiga L., 2017, MNRAS, 468, 597
- [207] Roming P.W., 2005, Space Sci. Rev., 120, 95
- [208] Tavecchio F., Ghisellini G., 2015, MNRAS, 451, 1502
- [209] Taylor M. B. 2005, Astronomical Data Analysis Software and Systems XIV, 347, 29
- [210] Urry C. M., Padovani P., 1995, PASP, 107, 803

